THE UNIVERSITY OF CHICAGO

INVESTIGATION OF CHEMICAL PATTERN DESIGN AND BLOCK COPOLYMER FORMULATION ON DIRECTED SELF-ASSEMBLY

A DISSERTATION SUBMITTED TO

THE FACULTY OF THE INSTITUTE FOR MOLECULAR ENGINEERING

IN CANDIDACY FOR THE DEGREE OF

DOCTOR OF PHILOSOPHY

BY

LANCE DAVID WILLIAMSON

CHICAGO, ILLINOIS

DECEMBER 2015

CONTENTS

LIST OF FIGURES v

LIST OF TABLES x

ACKNOWLEDGEMENTS xi

ABSTRACT xii

Chapter 1: Introduction 1

1-1 Overview of block copolymers 1

1-2 Thin films of block copolymers 1

1-3 Directed self-assembly of block copolymers 2

1-4 Blends including BCP 4

1-5 Outline of the thesis 5

1-6 References 7

Chapter 2: Three-tone Chemical Patterns for Block Copolymer Directed Self-Assembly 10

2-1 Abstract 10

2-2 Introduction 11

2-3 Experimental Section 13

2-4 Results and Discussion 15

2-5 Conclusion 34

2-6 References 34

Chapter 3: Influence of Guide Stripe Composition on DSA 38

3-1 Abstract 38

3-2 Introduction 38

3-3 Experimental Section 40

3-4 Results and Discussion 41
3-5 Conclusion 50
3-6 References 51
Chapter 4: Impact of BCP Asymmetry on DSA Patterning Performance 53
4-1 Abstract 53
4-2 Introduction 53
4-3 Experimental Section 55
4-4 Results and Discussion 57
4-5 Conclusion 67
4-6 References 68
Chapter 5: Macrophase Separation of Blends of Diblock Copolymers in Thin Films 70
5-1 Abstract 70
5-2 Introduction 71
5-3 Experimental Section 72
5-4 Results and Discussion 74
5-5 Conclusion 87
5-6 References 88
6: Conclusion 91

LIST OF FIGURES

Figure 2-1. (a) Schematic representation of processing steps, including chemical pattern fabrication and BCP DSA. (b) Top-down SEM images show the X-PS stripe and resist after trim etch. (c) The cross-sectional schematic of the expected X-PS structure. 17

Figure 2-2. Characterization of the X-PS stripe geometry for a series of guide stripe widths W. GISAXS spectra in (a) were used to determine the slope of the sidewall, converted from reciprocal space to real space in (b). SEM images (c) were used to measure W after trim and confirm the presence of broad sidewalls on the X-PS structures. Stripe dimensions are summarized in (d). For the largest two guide stripe widths, the sidewalls merge and no SiN is visible, so the dimensions marked with † are based on gap width. 20

Figure 2-3. Unpatterned surfaces were processed with the steps described in Figure 1 to emulate the regions of the chemical pattern. The sidewall surface is simulated by etching partway through a thick coat of X-PS. Water contact angle measurements in (a) are associated with different regions of the chemical pattern, schematically illustrated from the top-down perspective in (b). Two BCP's were assembled on each surface in (c-d); the left, middle and right columns correspond to backfill, sidewall, and top surfaces, respectively. A symmetric BCP in (c) has PS-preferential wetting on the top of the guide stripe while a PS-rich lamellae-forming BCP in (d) has PMMA-preferential wetting on the sidewall. All other combinations resulted in perpendicular lamellae, indicative of non-preferential wetting. 25

Figure 2-4. SEM images after trim etch and PMMA etch as W increases from (a) to (e). Three separate ranges (a), (c), and (e) lead to ordered arrays of BCP separated by ranges (b) and (d) corresponding to no pattern registration. 29

Figure 2-5. A BCP formulation that exhibits dense PS microbridges on (a) unpatterned brush, (b) overetched X-PS stripe, (c) guide stripe ~0.5 L_0, (d) guide stripe ~1.5L_0. In all cases, PS microbridges form over backfill brush rather than over plasma-treated X-PS sidewall.....31

Figure 3-1. Schematic of process flow for fabricating the chemical patterns and assembling BCP. 42

Figure 3-2. Water contact angle of each GSM before and after processing to simulate the guide stripe surface. Lower water contact angles correspond to less PS-preferential surfaces. 43

Figure 3-3. Geometric commensurability is assessed for different guide stripe compositions after 1 min of anneal. Fields with perfect registration in the representative field of view are marked green. An axis-aligned ellipse is fit to the data to describe the range of guide stripe width and pitch commensurability. The range of commensurability in width and pitch are the major and minor axes of the ellipse. 44

Figure 3-4. (a) Sample image with 20% fraction misalignment marking the aligned BCP in blue and misaligned BCP in red. (b) The fraction of misalignment through guide stripe width at optimum pitch. (c) The gradient in the misalignment area for the series of GSM. A steeper transition to the ordered regime is observed for a more preferential guide stripe (higher %PS). .46

Figure 3-5. (a) Geometric commensurability after 1, 5 min and 4 hr BCP anneal. (b) Fraction of misalignment for 100% PS GSM after 1 min and 4 hr BCP anneal. Additional annealing increases the number of defect-free fields, but does not alter the maximum commensurability tolerance. 48

Figure 3-6. Line edge roughness comparing DSA performance on the series of GSM. 49

Figure 4-1. The domain spacing and overall volume fraction of PS change for BCP + HP binary blends. Error bars represent the standard deviation of the measurements. 57

Figure 4-2. Schematic of processing steps used to fabricate chemical patterns and assemble BCP. 58

Figure 4-3. BCP registration quality is plotted through a range of guide stripe dimensions with respect to BCP formulation asymmetry and backfill brush composition. All fields are distinguished as defect-free (green) or containing misregistration defects (red) in a representative SEM image. An axis-aligned ellipse marks the transition for each set of processing conditions and the range of the major and minor axis of each ellipse is color-coded from largest (green) to smallest (red). 60

Figure 4-4. Formulation kinetics process window for pattern registration defined by 1 SEM image per field. All formulations show an improved range of assembly between 1 minute and 5 minutes, but 4 hours of annealing does not lead to substantial improvement in commensurability tolerance range. An axis-aligned ellipse marks the transition for each set of processing conditions and the range of the major and minor axis of each ellipse is color-coded from largest (green) to smallest (red). 62

Figure 4-5. DSA misregistration-style defect categories are represented schematically and with example images. The left column only involves configurations of dislocation pairs whereas the right column always includes at least one disclination. 64

Figure 4-6. Defect review and classification identified misregistration defect modes through pitch at best guide stripe width. The conditions resulting in large commensurability tolerance are bounded by the dislocation-style defect whereas conditions resulting in narrower commensurability tolerance have predominantly disclination-style defects at the limit of assembly. 65

Figure 4-7. Microbridges were present after pattern transfer to Si, which were not observed after PMMA removal. The density of microbridges is a function of backfill composition, BCP composition, guide stripe width and pitch. 66

Figure 5-1. Representative SEM images of each blend series at different volume fractions spanning the composition range of macrophase separation. The red highlighted images have macrophase separation. The blue highlighted images show transition behavior. The circles indicate swelled junctions in a transition behavior from miscible blend series to macrophase separating series. 76

Figure 5-2. The domain spacing for SM211/SM44 $\varphi L = 0.3$ was measured by two techniques: 1. Using FFT by calculating the FFT power spectrum (B) from the SEM image (A), then averaging the power spectrum (C) and identifying the primary peak(s). 2. Real-space measurement was achieved by identifying low-curvature segments and measuring the distance across multiple periods (A). Both techniques were repeated to average the domain spacing. 77

Figure 5-3. Period analysis and modeling of blends with respect to composition for (A) miscible blend series SM129/SM44 and SM211/SM44, and (B) macrophase separating series SM320/SM44 and SM412/SM44. Error bars indicate one standard deviation of error. 79

Figure 5-4. The area fraction of the large period phase (a_L) is measured by manually defining the phase boundary in Axiovision software (A). The area fraction of the large period phase is given with respect to the blend fraction for SM412/SM44(squares) and SM320/SM44(diamonds) (B). A linear relationship is expected for standard thermodynamic two-phase equilibria. The small period phase is nearly pure of the short block copolymer and the large period phase is less than $\varphi L = 0.5$ for both blend series. 81

Figure 5-5. SAXS traces of bulk PS-b-PMMA blends at different blend fractions taken at room temperature after annealing. Peaks designated with a prime correspond to a separate small period phase. 84

Figure 5-6. Phase diagram of the BCP-BCP macrophase separation for thin film and bulk. Thin film phase boundary points are from area fraction analysis in Figure 4 extrapolated to the phase boundary. Bulk phase boundary points are from comparing the period of the phase separated domains to the miscible period analysis in Figure 5-3. Lines guide the eye through the phase boundary points.....85

Figure 5-7. GISAXS spectra of SM412/SM44 $\varphi_L = 0.5$ at different film thicknesses and incident angles. While the 60 nm film has no indication of small period phase, the thicker films have a coexistence of both phases. 87

LIST OF TABLES

Table 5-1. Characteristics of PS-*b*-PMMA.....72

Table 5-2. Comparison of the period of each phase for the film and bulk samples.....82

ACKNOWLEDGEMENTS

My PhD has been much more of an adventure than what I expected when I began in Madison, WI in 2009. I want to thank the many people that have come along beside me on my journey.

First and foremost, I am grateful to my advisor, Professor Paul Nealey. He has guided, stimulated, and enabled me to grow academically and professionally. He fostered a creative environment both within the Nealey research group and through collaborations around the world.

I have worked with and learned from many graduate students and post-doctoral scholars, both in the Nealey research group as well as through several collaborations. Science is certainly a team venture. In particular, Robert Seidel has been a close colleague and we have had an uncountable number of insightful discussions that has shaped my understanding of scientific phenomena.

I acknowledge Geoff Brennecka and everyone that I worked with and learned from in the NINE program. I gained valuable experience learning the principles of immersion lithography from Alex Raub on his custom-built optics system in the Steven Brueck group. I also learned the hard way how innocuous-looking changes to a system can have drastic consequences to the final outcome.

I appreciate the opportunity to join Roel Gronheid's research group at imec. In particular, the DSA team, but advanced patterning in general. Special thanks to the AZ/Merck team for providing materials for my formulation projects and for BT Chan and Doni Parnell for plasma etch development.

Family and friends have also been very supportive. My parents, Lyle and Sondra Williamson have encouraged me through all of my academic pursuits.

ABSTRACT

Directed self-assembly (DSA) of block copolymer (BCP) films is in development to augment advanced lithography capabilities. By combining state-of-the-art lithography techniques to guide the thermodynamically driven self-assembly, well-ordered arrays of nanoscale structures can be achieved over macroscopic dimensions. Both the design of the block copolymer and the substrate have tremendous impact on the properties of the self-assembled film.

In chapters 2-4, chemoepitaxial surface patterns are used to direct the BCP; they are composed of guide stripe and background regions that are designed so that the minimum free energy of the system is achieved when the lamellae are aligned to the stripes. Chapter 2 characterizes a novel architecture for chemical patterns, where three separate regions of the pattern contain distinct wetting behavior; the guide stripe formed a trapezoidal cross-section and the sidewalls have distinct wetting behavior compared to the guide stripe and the background. Chapter 3 examines the role of the chemistry of the guide stripe material, which influences the interfacial energy between the guide stripe and the BCP domain in contact with it. The guide stripe ideally makes the largest difference in interfacial energy with respect to the BCP chemistries. Less selective guide stripes impose a weaker driving force for DSA and therefore have slower assembly kinetics.

The properties of block copolymers can be tuned by blending homopolymers (HP) or other block copolymers. Binary blends of BCP and HP are used in Chapter 4 as a proxy for modifying the overall volume fraction of the BCP during DSA. Whereas the behavior of unpatterned BCP behavior is symmetric with volume fraction, the asymmetry stabilizes different defect mechanisms in DSA depending on whether the majority or minority block is guided by the

chemical pattern. PMMA-rich formulations stabilized disclination-style defects due to weaker pattern registration whereas PS-rich formulations formed microbridges that interfered with pattern transfer. Chapter 5 characterizes the macrophase separation behavior of BCP-BCP blends in thin films; Macrophase separation occurs in symmetric BCP of matching polymer chemistries when the ratio of the molecular weights is at least five and the volume fraction of short BCP is high enough to saturate the interface of the long BCP. This critical composition of macrophase separation is different in thin film compared to the bulk, which influences not only the amount of each phase as determined by the lever rule, but also the period of the large period phase as determined by the miscible blend scaling equation.

Chapter 1:

Introduction

1-1 Overview of Block Copolymers

Block copolymers (BCP) are polymers composed of more than one monomer chemistry that are clustered into blocks. Repulsion between the covalently bonded blocks leads to microphase separation, where the blocks organize into periodic arrays of domains that minimize the interfacial area between the chemistries. For diblock copolymers, the bulk morphology is governed by the volume fraction (f), the Flory-Huggins interaction parameter (χ), and the degree of polymerization (N).[1] Arrays of lamellae, cylinders or spheres can minimize the interfacial area for increasingly asymmetric BCP's, respectively. The periodicity of the microdomains is dictated by a balance between the repulsion of the blocks and the entropic tendency for each chain to adopt a random coil configuration. This work exclusively uses lamellae-forming poly(styrene-*block*-methyl methacrylate) (PS-*b*-PMMA) diblock copolymers.

1-2 Thin Films of Block Copolymers

Confinement of block copolymers in thin films introduces new parameters to the system. One key characteristic of a BCP film is the orientation of the microdomains, as perpendicular lamellae and cylinders have great potential for nanopatterning applications. The interfacial energy of the BCP with the substrate and the relative surface energy of the blocks at the free surface have a strong influence on the morphology. When one of the BCP chemistries has a lower free energy at a surface, it will form a wetting layer. Since PS and PMMA have similar surface energies in the melt, both domains can be present at the free surface; in this case, the

wetting behavior of the substrate controls the orientation of the microdomains in the film.[2] One approach to controlling the wetting behavior of the BCP with the substrate is to modify the surface by grafting or crosslinking a polymer.[3] Whereas a pure PS- or PMMA-modified substrate wets the respective block of the BCP, a PS-*r*-PMMA random copolymer surface can be non-preferential between the domains, thus drive the microdomain interface perpendicular to the substrate. In particular, the ideal composition of the random copolymer to achieve this wetting behavior depends on the relative amount of each BCP chemistry in the overlying polymer. The microdomain orientation in thin films is also dependent on film thickness.[4] Films commensurate in thickness to the stacking of lamellae stabilize the parallel orientation because films with thicknesses incommensurate to the natural periodicity result in terracing when the lamellae are parallel to the substrate. This structure leads to additional free surface area that contributes additional surface energy compared to a film of commensurate thickness. For this reason, the range of surfaces that lead to perpendicular orientation changes with film thickness.

1-3 Directed Self-assembly of Block Copolymers

A non-preferential surface generates perpendicularly aligned features, but much of the technological usefulness of these films, namely use as a lithographic mask, depends on achieving long-range order and control of the feature alignment through directed self-assembly (DSA). Two general approaches are commonly used to organize the BCP domains into long-range arrays with positional control. Graphoepitaxy[5] uses topographic features to confine the polymer whereas chemoepitaxy[6] is based on chemical patterns that designed to minimize the interfacial energy with the BCP when the domains are aligned to regions of different polymer wetting behaviors. Chemical patterns are composed of guide stripe regions preferential to one of the

domains separated by background regions that minimize the interfacial energy with the remaining domains.[7]

The design parameters of the chemical pattern that are critical for BCP DSA include the periodicity of the chemical pattern, width of the guide stripe, and wetting behavior of the BCP chemistries with the patterned regions.[8] The optimum periodicity of the chemical pattern is an integer multiple of the BCP natural periodicity, but the BCP can stretch or compress to accommodate some incommensurability. The number of BCP features that assemble per guided feature is the density multiplication factor; larger values give more resolution enhancement at the cost of driving force.[9] The ideal guide stripe width matches the width of one domain. Note that if the pattern periodicity stretches or compresses the domains compared to the natural fingerprint spacing, the guide stripe dimension should be matched to the patterned BCP dimensions rather than the natural dimensions of the BCP. Also, DSA has been demonstrated for guide stripe widths of $(n+1/2)L_0$, although non-through-film structures may result in this regime. The ideal wetting behavior of each surface of the chemical pattern is dependent on the geometric design.[7] Similar to unpatterned surfaces, the continuum of wetting behaviors can be accessed using random copolymers and the ideal composition is proportional to the composition of the BCP domains above that region of the chemical pattern.

In addition to the design of the chemical pattern, factors such as BCP film thickness, anneal time, and anneal temperature are also critical to consider regarding DSA performance. Thinner BCP films lead to a proportionally larger free energy contribution from the chemical pattern.[8] Also, assembly kinetics have been shown to follow an Arrhenius temperature dependence that is only limited by polymer decomposition.[10] Reasonably designed DSA systems have been

predicted to have an enormous free energy penalty for misalignment so any observed misalignment including dislocation pairs and disclinations are regarded as kinetically trapped states that would align if the system were given sufficient mobility.[11-12]

1-4 Blends Including BCP

On top of all of the variety displayed by uniform diblock copolymers, more complexity and possibilities are unveiled through blends of polymers including diblock copolymers. For example, blending a homopolymer with a diblock copolymer substantially increases the complexity of the phase behavior and the number of parameters that define the system.[13] In addition, the equilibrium structures of homopolymer/diblock copolymer blend films, including conditions when the homopolymer is dissimilar to either block has been explored through Monte Carlo simulations.[14] By adding homopolymer of both polymers composing a diblock copolymer was studied, maintaining a symmetric blend of homopolymers.[15-16] As the fraction of homopolymer increases, the mode of polymer segregation changes from microphase, microemulsion, and then macrophase. Blending block copolymers with homopolymers has proven to be advantageous to the directed assembly on chemical patterns by improving the stability of curvature in the assembled lamellae.[17-18]

Just as block copolymer/homopolymer blends add new dimension, blends of block copolymers also display novel characteristics. Mixing symmetric block copolymers of different molecular weights results in a single natural lamellar period.[19] In addition, thin films of this style of polymer blend have been directed to assemble on chemical patterns matching each blends' bulk period.[20] When the block copolymers in the blend are not symmetric, several specific regimes must be considered. Complimentarily asymmetric block copolymer blends can span different

morphologies, depending on the blend ratio.[21-22] In addition, spheres of different sizes can coexist without a distinct phase boundary, and cylinders of one polymer and spheres of the other in equilibrium, segregated into phases on the micron size scale.[23] More detailed analyses focus on macrophase separation of symmetric block copolymers; sufficiently disparate molecular weights can lead to macrophase separation, characterized by a large period lamellae phase and a small period lamellae phase.[24-25] More specifically, the critical molecular weight ratio for phase separation is five and the blend must be composed of at least 40% of the small block copolymer.[26] Also, the miscibility of lamellae is temperature-dependent, such that an increase in temperature can change a polymer mixture from macrophase separating into two lamellae periods to single period lamellae.[27] The grain boundary between the phases has been proposed to be a Scherk's first surface, such that both phases are continuous from one period phase to the other.[28] Dynamic simulation of these blends demonstrates that the different chemistries separate quickly, followed by a simultaneous structuring of the lamellae and grain boundaries between periodicity phases.[29] Simulations of blends involving a symmetric and an asymmetric block copolymer display an assortment of morphologies, depending on the interaction parameter, ratio of molecular weights and feed ratio of the polymers in the blend.[30]

1-5 Outline of the Thesis

Many design parameters need to be explored and understood before BCP DSA can meet the performance standards required for high-volume manufacturing. Performance metrics include defect density and line roughness, which are affected by many system parameters in the chemical pattern and the BCP formulation.

Chapter 2 describes an innovative chemical pattern design for density multiplication that has three surfaces with distinct wetting behavior including the resist-protected guide-stripe, plasma-modified sidewall, and a background brush. These patterns guide three times as many BCP domains as a traditional pattern of the same resolution of photolithography template. The geometry and wetting behavior of the chemical pattern components are assessed and BCP DSA behavior is addressed in the context of this pattern architecture.

Chapter 3 addresses the role of the guide stripe material chemistry using a series of PS-rich random copolymer mats. When the composition of the guide stripe becomes less preferential to the guided domain, the kinetics to achieve well-ordered domains are slower and the line edge roughness in the final array is larger. This study emphasizes the importance of achieving strongly preferential guide stripes in order to attain the best performance metrics.

Chapter 4 probes the effects of asymmetric lamellae-forming BCP on chemical patterns using binary blends of a symmetric BCP and one homopolymer. Previous work has demonstrated that the unguided behavior of this style of formulation is symmetric with volume fraction; however this study encounters different behavior for the PS- and PMMA-rich systems. The PS-rich blend forms non-through-film microbridge structures across the PMMA domain whereas the PMMA-rich blend has weaker pattern registration leading to a stabilization of disclination-style defects and a narrower commensurability tolerance. The PMMA-rich DSA behavior was verified with an intentionally asymmetric BCP to confirm that this observation is not an artifact of the formulation. This study demonstrates that the DSA quality is very sensitive to the BCP composition.

Chapter 5 characterizes the effect of thin film confinement of macrophase separation for a blend of symmetric diblock copolymers of disparate molecular weight. The thin film confinement increases the miscible blend range, which is present even for films much thicker than the microdomain scale. This shift in the phase diagram changes not only the expected amount of each phase, as given by the lever rule but also the period of the large period phase, which is determined by the miscible domain scaling equation evaluated at the saturation composition. BCP thin films with multiple periodicities provide new possibilities for future applications.

1-6 References

1. Khandpur, A. K.; Forster, S.; Bates, F. S.; Hamley, I. W.; Ryan, A. J.; Bras, W.; Almdal, K.; Mortensen, K. *Macromolecules* **1995**, 28(26), 8796-8806.

2. Mansky, P.; Liu, Y.; Huang, E.; Russell, T. P.; Hawker, C. *Science* **1997**, 275(5305), 1458-1460.

3. Han, E.; Stuen, K. O.; La, Y.-H.; Nealey, P. F.; Gopalan, P. *Macromolecules* **2008**, 41(23), 9090-9097.

4. Suh, H. S.; Kang, H.; Nealey, P. F.; Char, K. Macromolecules 2010. 43(10), 4744-4751.

5. Han, E.; Kang, H.; Liu, C. C.; Nealey, P. F.; Gopalan, P. *Advanced Materials* **2010**, 22(38), 4325-4329.

6. Edwards, E. W.; Montague, M. F.; Solak, H. H.; Hawker, C. J.; Nealey, P. F. *Advanced Materials* **2004**, 16, (15), 1315-1319.

7. Liu, C.-C.; Ramirez-Hernandez, A.; Han, E.; Craig, G. S. W.; Tada, Y.; Yoshida, H.; Kang, H.; Ji, S.; Gopalan, P.; de Pablo, J. J.; Nealey, P. F. *Macromolecules* **2013**, 46, (4), 1415-1424.

8. Delgadillo, P. A. R.; Harukawa, R.; Parnell, D.; Lee, Y.-T.; Chan, B. T.; Lin, G.; Cao, Y.; Nagaswami, V. R.; Somervell, M. H.; Nafus, K.; Gronheid, R.; Nealey, P. F. *SPIE Advanced Lithography* **2014**, 9049, 9049-19.

9. Liu, G.; Delcambre, S. P.; Stuen, K. O.; Craig, G. S. W.; de Pablo, J. J.; Nealey, P. F. *J. Vac. Sci. Technol. B* **2010**, 28(6), C6B13-C6B20.

10. Welander, A. M.; Kang, H.; Stuen, K. O.; Solak, H. H., Muller, M. de Pablo, J. J.; Nealey, P. F. *Macromolecules* **2008**, 41(8), 2759-2761.

11. Nagpal, U.; Mueller, M.; Nealey, P. F.; de Pablo, J. J. *ACS Macro Lett*. **2012**, 1, (3), 418-422.

12. Li, W.; Nealey, P. F.; de Pablo, J. J.; Mueller, M. *Phys. Rev. Lett*. **2014**, 113, (16), 8301-8301.

13. Matsen, M.W. *Macromolecules* **1995**, 28(17), 5765-5773.

14. Huang, Y., H. Liu, and Y. Hu. *Macromol. Theory Simul*. **2006**, 15(4), 321-330.

15. Liu, G.; Stoykovich, M. P.; Ji, S.; Stuen, K. O.; Craig, G. S. W.; Nealey, P. F. *Macromolecules* **2009**, 42(8), 3063-3072.

16. Stuen, K.O.; Thomas, C. S.; Liu, G.; Ferrier, N.; Nealey, P. F. *Macromolecules* **2009**, 42(14), 5139-5145.

17. Stoykovich, M.P.; Muller, M.; Kim, S. O.; Solak, H. H.; Edwards, E. W.; de Pablo, J. J.; Nealey, P. F. *Science* **2005**, 308(5727), 1442-1446.

18. Liu, G.; Thomas, C. S.; Craig, G. S. W.; Nealey, P. F. *Adv. Funct. Mater*. **2010**, 20(8), 1251-1257.

19. Mayes, A.M.; Russell, T. P.; Deline, V. R.; Satija, S. K.; Majkrzak, C. F. *Macromolecules* **1994**, 27(25), 7447-7453.

20. Edwards, E.W.; Stokyovich, M. P.; Nealey, P. F.; Solak, H. H. *J.Vac. Sci. Technol. B* **2006**, 24(1), 340-344.

21. Yamaguchi, D.; Takenaka, M. Hasegawa, H.; Hashimoto, T. *Macromolecules* **2001**, 34(6), 1707-1719.

22. Chen, F., Y. K.; Hashimoto, T. *Macromolecules* **2007**, 40(10), 3714-3723.

23. Koizumi, S.; Hasegawa H.; Hashimoto, T. *Macromolecules*, **1994**. 27(15), 4371-4381.

24. Hashimoto, T.; Yamasaki, K.; Koizumi, S.; Hasegawa, H. *Macromolecules* **1993**, 26(11), 2895-2904.

25. Papadakis, C.M.; Mortensen, K.; Posselt, D. *Eur. Phys. J. B* **1998**. 4(3), 325-332.

26. Yamaguchi, D.; Hashimoto, T. *Macromolecules* **2001**, 34(18), 6495-6505.

27. Yamaguchi, D.; Hasegawa, H.; Hashimoto, T. *Macromolecules* **2001**, 34(18), 6506-6518.

28. Hashimoto, T.; Koizumi, S.; Hasegawa. H. *Macromolecules* **1994**, 27(6), 1562-1570.

29. Morita, H.; Kawakatsu, T.; Doi, M.; Yamaguchi, D.; Takenaka, M.; Hashimoto, T. *Macromolecules* **2002**, 35(19), 7473-7480.

30. Wu, Z.; Li, B.; Jin, Q.; Ding, D. *Macromolecules* **2011**, 44, 1680-1694.

Chapter 2:

Three-tone Chemical Patterns for Block Copolymer Directed Self-Assembly

2-1 Abstract

Chemical patterns for directed self-assembly (DSA) of lamellae-forming block copolymers (BCP) with density multiplication can be fabricated by patterning resist on a cross-linked polystyrene layer, etching to create guide stripes, and depositing end-grafted brushes in between the stripes as background. To date, two-tone chemical patterns have been targeted with the guide stripes preferentially wet by one block of the copolymer and the background chemistry weakly preferentially wet by the other block. In the course of fabricating chemical patterns in an all-track process using 300 mm wafers, it was discovered that the etching process followed by brush grafting could produce a three-tone pattern. We characterized the three regions of the chemical patterns with a combination of SEM, glancing-incidence small-angle x-ray scattering (GISAXS), and assessment of BCP wetting behavior, and evaluated the DSA behavior on patterns over a range of guide stripe widths. In its best form, the three-tone pattern consists of guide stripes preferentially wet by one block of the copolymer, each flanked by two additional stripes that wet the other block of the copolymer, with a third chemistry as the background. Three-tone patterns guide three times as many BCP domains as two-tone patterns and thus have the potential to provide a larger driving force for the system to assemble into the desired architecture with fewer defects in shorter time and over a larger process window.

2-2 Introduction

Devising strategies to multiply the density of features derived from 193 nm immersion lithography templates dominates current research and development of semiconductor patterning.[1] One approach uses block copolymers (BCP) that self-assemble into periodic arrays of nanoscale features.[2] Precise placement and orientation of these nanoscale features can be obtained through directed self-assembly (DSA).[3] In chemoepitaxial DSA of lamellae-forming block copolymers in line/space arrays, the BCP film is assembled on lithographically defined chemical patterns consisting of guide stripes and background regions that direct the registration of assembled BCP domains.[4-8] The perfection of registration and control of through-film morphology depends on key parameters of the chemical pattern: the width and periodicity of the guide stripes and the chemistry of the guide stripes and background regions.[9-11] Optimally, the guide stripes are the width of one lamellar domain, the pattern chemistries are selected to minimize the interfacial energy between the BCP and the chemical pattern, and the guide stripe periodicity, L_S, is an integer multiple of the natural period of the block copolymer, L_0. In this way chemoepitaxial DSA with density multiplication enables sub-resolution extension of lithographic patterning.

Liu et al.[12] developed a method to fabricate chemical patterns with independent control over each of the key pattern attributes described above. In one specific implementation of this process, as applied towards directing the assembly of poly(styrene-*block*-methyl methacrylate) (PS-*b*-PMMA), a crosslinked polystyrene (X-PS) mat is deposited on a silicon wafer, and photoresist is patterned on top of the mat. The resulting structures are treated with a plasma trim etch that laterally shrinks the photoresist lines and removes X-PS in the spaces between them. The remaining photoresist is stripped and the spaces are backfilled by grafting an end-functional

random copolymer brush P(S-*r*-MMA) of tunable composition, resulting in a two-tone pattern of sparse X-PS guide stripes and background brush regions. The optimum composition of the brush minimizes the interfacial energy of the substrate with the overlying BCP film and is a function of the degree of density multiplication. This specific example of an X-PS guided system of P(S-b-MMA) has been used extensively in past work, and the flow has been generalized for use with many different BCP systems by changing the guiding mat and background materials.[13, 14] The key attribute of the flow is to control all of the critical parameters independently, since the pitch and width of the photoresist features after lithographic patterning combined with the trim etch process control the geometry of the pattern, and materials chosen for the mat and brush determine its chemistry. These 'two-tone' surface patterns have been used extensively to understand the fundamental science behind directed assembly in the laboratory. The full DSA process has been implemented as the Liu-Nealey (LiNe) flow for all-track processing using 193 nm immersion lithography at imec (Leuven, Belgium) using solvents and processes that are compatible with 300 mm tools.[15]

In the course of investigating the materials and process conditions in this flow using high-volume manufacturing tools, we discovered a method to fabricate 'three-tone' rather than 'two-tone' chemical patterns. The three-tone patterns consist of PS-wetting guide stripes, each flanked by PMMA-wetting sloped sidewalls, with polymer brushes of a third chemistry in the background spaces. Three-tone chemical patterns present a potential advantage over two-tone patterns because they guide three times as many BCP domains towards the desired domain architecture. Past work has shown that a higher fraction of guided domains results in faster annealing kinetics,[16] suggesting that this type of pattern may better enable DSA to meet

requirements for high-volume manufacturing. We characterized the geometry of the three-tone patterns using grazing-incidence small-angle X-ray scattering (GISAXS) and the chemistry of the regions of the pattern with various techniques. Finally, we discuss the implications for improvement of DSA using three-tone chemical patterns.

2-3 Experimental Section

A. Materials:

Crosslinking polystyrene (X-PS) (AZEMBLY^{TM} NLD-128), P(S-*r*-MMA) brush (AZEMBLY^{TM} NLD-127, 51% PS), P(S-*b*-MMA) BCP with L_0 = 28 nm (AZEMBLY^{TM} PME-312) and a P(S-*b*-MMA) BCP formulation (L_0 = 28.5 nm) engineered to form microbridges were provided by Merck Performance Materials. ArF photoresist AIM5484 was purchased from JSR Micro. Orgasolv STR 301 was purchased from BASF. Organic solvent RER600 was purchased from Fujifilm.

B. Chemical pattern fabrication and BCP assembly:

The chemical patterns were fabricated on a 300 mm process line devoted to DSA at the imec nanoelectronics R&D lab in Belgium.[15] A 13 nm silicon nitride (SiN) film was deposited on 300 mm Si wafers as an inorganic antireflective coating. The wafers were coated with an 8 nm spincast film of X-PS, and then annealed at 315 °C for 5 min in a nitrogen environment using a TEL CLEAN TRACK ACT^{TM}12 track. The wafers were coated with AIM5484 (95 nm) using a SOKUDO DUO track, exposed on an ASML 1950 immersion scanner (optimum dose = 11 mJ, optimum focus = -0.02 μm, NA = 1.35, dipole illumination, σ_o = 0.98, σ_i = 0.86, blade angle = 40°) and developed to create 84 nm pitch line-space patterns of various line widths. The samples were etched with oxygen-containing plasma, which simultaneously isotropically etched the

photoresist and removed unprotected X-PS. The remaining resist was stripped with Orgasolv STR 301, leaving isolated X-PS stripes on the nitride. The pattern was coated with backfill brush AZEMBLY^{TM} NLD-127 (50 nm), then annealed for 5 min at 250 °C to graft the brush to the nitride surface. The remaining ungrafted brush was removed through rinsing with RER600, leaving a chemical pattern of alternating X-PS stripes and backfill brush regions. BCP was spin-coated at a thickness of 35 nm and annealed at 250 °C with nitrogen purge for various times. The PMMA domains were removed with plasma etching on a TEL Tactras^{TM} for better SEM contrast.

C. Unpatterned surface (designed to emulate regions of chemical pattern) preparation:

For areas representative of the guide stripe top and brush regions, wafers were coated with X-PS according the process described above. Large (> 1 in^2) exposed and unexposed areas were patterned and developed, and then the wafers were processed according to the remainder of the treatment above. The unexposed regions (protected by photoresist during the trim etch process) were therefore large areas of unmodified X-PS, whereas the exposed regions were large areas of grafted backfill brush.

To create a large area surface of similar chemistry to that of the sidewall, the following procedure was implemented. X-PS was coated, then lightly crosslinked at 250 °C for 1 minute. This coating procedure was repeated five times, for a total thickness of 32 nm, and then the whole stack was thoroughly crosslinked using the standard bake of 5 minutes at 315 °C. Alternating exposed and unexposed areas were patterned and developed as described above, and the wafers were trim etched. The trim etch process, however, only removed ~12 nm of the thick

X-PS film, leaving ~20 nm of plasma-modified polystyrene in the exposed areas. The treatment then proceeded in the standard manner, with photoresist strip and brush grafting.

D. Characterization:

Grazing incidence small angle x-ray scattering (GISAXS) was performed at Sector 8-ID-E of the Advanced Photon Source at Argonne National Laboratory. The measurements were taken under vacuum with an incident x-ray beam of 7.35 keV. The 5 mm x 7.5 mm block of 84 nm pitch pattern was aligned so that the X-PS stripes were parallel to the x-ray beam. The incidence angle was set at 0.2° a Pilatus CCD detector placed 2.17 m from the sample. The 2D GISAXS spectra are the sum of 30 one-second exposures collected.

Scanning electron microscope (SEM) imaging was performed with a Hitachi CG5000 after trim etch and after PMMA domain removal. The line width of the photoresist structures after trim etch, W, was measured by automated built-in Hitachi software and user verified with image-by-image inspection. Film thicknesses were determined with a KLA Tencor Aleris^{TM} 8330 spectroscopic ellipsometer. Static water contact angle measurements were obtained using a Dataphysics OCAH230L contact angle measurement system. A syringe dispensed 5 μL drops of deionized water, which were measured after 0.3 s of stabilization. In addition, BCP was coated and annealed as described above, then imaged with a Hitachi CG5000 SEM.

2-4 Results and Discussion

The process to generate chemical patterns for the directed self-assembly (DSA) of block copolymers (BCP) is shown schematically in Figure 1a. Photoresist is patterned on top of a crosslinked polystyrene (X-PS) mat using 193 nm immersion lithography, and then the photoresist lines are plasma trim etched and solvent stripped to leave a pattern of X-PS stripes at

84 nm pitch. An end-functional P(S-*r*-MMA) (51% PS) brush-forming polymer is coated on the pattern. The samples are annealed to allow the brush to graft to the spaces between the stripes. After excess brush material is rinsed off, a BCP film is deposited on the chemical pattern and assembled by thermal annealing. The period of the guide stripes (L_S) is an integer multiple of the BCP natural periodicity (L_0); the BCP domains interpolate between the guiding stripes of the chemical pattern to form arrays of regular structures at a higher density than the original chemical pattern. Figure 1a illustrates the process flow for 3x density multiplication of features.

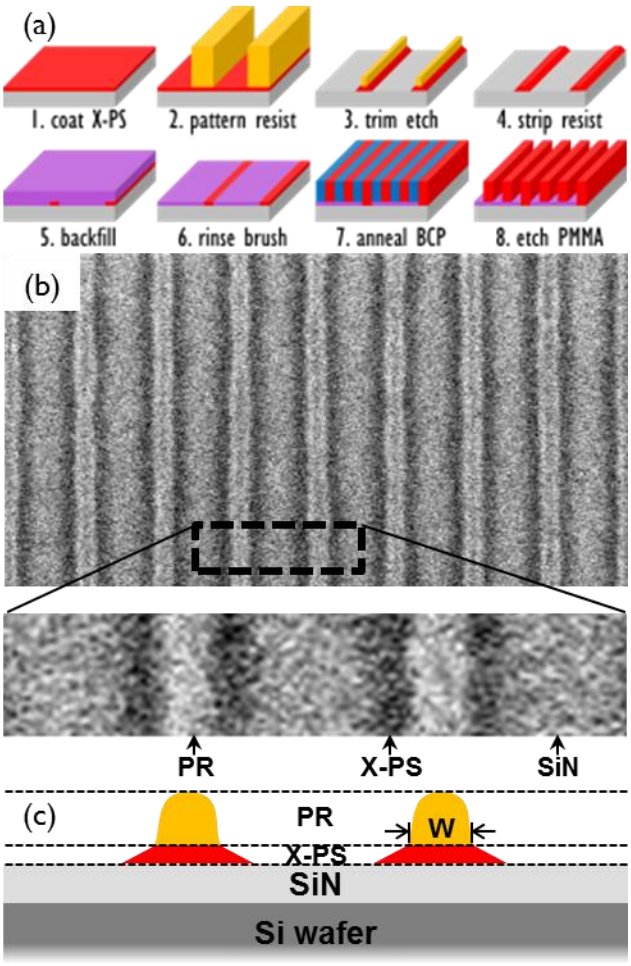

Figure 2-1. (a) Schematic representation of processing steps, including chemical pattern fabrication and BCP DSA. (b) Top-down SEM images show the X-PS stripe and resist after trim etch. (c) The cross-sectional schematic of the expected X-PS structure.

In order to better understand the guiding nature of the X-PS structures in the chemical patterns, it is imperative to carefully consider the effects of the processing steps used in generating these patterns. In particular, the trim etch process (step 3) has a significant impact on both the geometry and chemistry of these structures. During the trim etch process as implemented in the current process flow at imec, the patterned photoresist lines and the X-PS mat underneath them are exposed to an oxygen-containing plasma environment. This plasma treatment isotropically etches the photoresist structures and the unprotected X-PS mat; the etch rate of the photoresist,

however, is higher than that of the X-PS. As the photoresist lines shrink, additional X-PS is revealed and etched. When the etch process is complete, the three regions indicated in the top-down SEM images of Figure 1b are observed. The brightest regions are the remaining photoresist lines; the guide stripe width, W, is defined as the width of these lines. Since the etch is isotropic, the X-PS underneath is not a perfect vertical projection of the resist structures but "footing" can be seen as dark regions flanking each side of the remaining resist. Finally, the bare SiN wafer can be seen as a lighter region between the periodic resist/X-PS lines. In these samples, the X-PS adjacent to the unremoved resist has been plasma treated for a short time and is therefore only partially removed, whereas the X-PS exposed to the plasma from the beginning undergoes a longer etch time and is completely removed. This gradient of exposure time yields the trapezoidal structures represented schematically in Figure 1c.

We have been describing the tapered sidewalls of the trapezoidal structures as X-PS, but a careful consideration of the plasma etching process suggests that the surface of the partially etched X-PS has different properties than the resist-protected top surface. During the trim etch process, the X-PS is exposed to an oxygen-containing plasma that modifies and eventually removes it. The "footing" portions of the X-PS mat that are partially etched but not completely removed therefore undergo some degree of oxidation.[10] The chemistry of this sidewall is thus different both from the protected X-PS (the top of the trapezoidal guide stripe) and from the brush later in the process (step 5 in Figure 1a). Herein we explain how we characterized more fully the trapezoidal cross-section of the X-PS stripes as well as the wetting nature of each of the three surfaces (guide stripe top, plasma-modified sidewall, and backfill brush) present in these chemical patterns.

We characterized the shape of the X-PS structures after trim etch and before backfill as a function of the width of the photoresist after trim etch by grazing incidence small angle x-ray scattering (GISAXS) and SEM analysis as shown in Figure 2. SEM provides real-space imaging of discrete locations on the substrate, while GISAXS gives average information about the 3D structure across large areas. The range of X-PS structures in Figure 2 was achieved by changing the exposure dose during the patterning process. After trim etch, the remaining resist was stripped (step 4, Figure 1a) prior to the GISAXS experiment. In our GISAXS configuration, q_x is along the beam direction and parallel to the guide stripes, q_y is orthogonal to the guide stripes in the sample plane, and q_z is the sample normal.

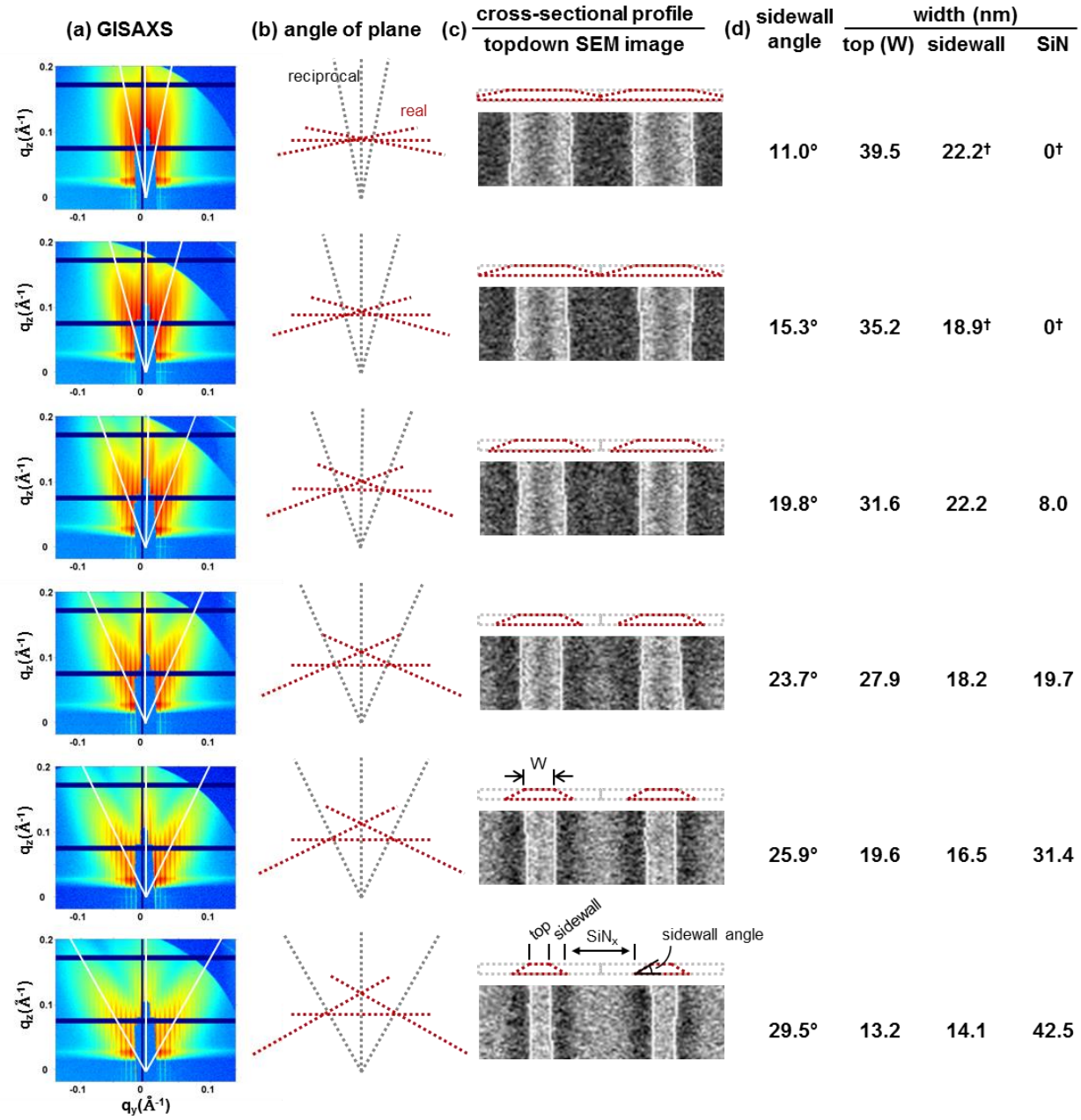

Figure 2-2. Characterization of the X-PS stripe geometry for a series of guide stripe widths W. GISAXS spectra in (a) were used to determine the slope of the sidewall, converted from reciprocal space to real space in (b). SEM images (c) were used to measure W after trim and confirm the presence of broad sidewalls on the X-PS structures. Stripe dimensions are summarized in (d). For the largest two guide stripe widths, the sidewalls merge and no SiN is visible, so the dimensions marked with † are based on gap width.

GISAXS patterns show the periodic sharp Bragg rods along the q_z direction for all samples. The pitch of the Bragg rods, 0.0075 $Å^{-1}$ in q_y, corresponds to an 83.8 nm pitch of the X-PS stripe, consistent with the 84 nm pitch targeted by lithography. These periodic Bragg rods are convoluted with the diffuse scattering in the background of the GISAXS patterns. The diffuse scattering is of highest intensity along three directions extending out from the origin of the detector in directions indicated by the white lines in Figure 2a, which correspond to three planes in real space normal to those directions in reciprocal space, as shown in Figure 2b. Thus, we estimate the sidewall angle from the angle of the diffuse scattering. The differences in the diffuse scattering patterns in Figure 2a indicate the varying shape of the X-PS structures illustrated in Figure 2c. The sidewall angle increases from 11.0^o to 29.5^o as the width of the photoresist structure after trim etch (defined as W) decreases from 39.5 nm to 13.2 nm, and can be attributed to the trim etch process. During the trim etch, a larger space between resist lines allows better access of the plasma to interact with the X-PS mat, resulting in a higher etch rate. Additionally, line-of-sight restrictions lead to higher etch rates near the center of the space compared to along the edge of the resist. These nonuniformity effects in the etch rate contribute to the difference in sidewall angle. Furthermore, upon breakthrough of the X-PS (when the underlying SiN stack is exposed), the added local loading density of the plasma species increases the lateral etching of the X-PS footing, further increasing the sidewall angle. It should be noted that in all cases, the sidewall angle was less than 30° and therefore quite shallow. Therefore, although we refer to these surfaces as "sidewalls," they are actually quite flat, with lateral dimensions on the lengthscale of BCP domain widths.

The overall dimensions of the X-PS structures can be estimated from the sidewall angles, resist widths (W), and thickness of X-PS (8 nm). The calculated sidewall width shown in Figure 2 is in agreement with the width of the darker region corresponding to the sidewall in top-down SEM images. The combination of GISAXS and SEM measurements give quantitative geometrical information about the trapezoidal X-PS structure. The widths of the three regions (unetched top of guide stripe, partially etched sidewall, and SiN) are listed in Figure 2d; for the widest guide stripes, the sidewalls merge and no SiN is uncovered.

In addition to characterizing the geometry of the X-PS stripes, we analyzed the wetting behavior of samples representative of each region of the chemical pattern by mimicking the processing steps on large-area surfaces. The chemical patterns consist of three regions: the top of the X-PS guide stripe protected by photoresist, the sidewall of the X-PS stripe exposed to the trim etch, and the brush region where X-PS was completely removed by the trim etch. In order to determine the wetting behavior of each of the three regions of the chemical pattern, large areas of X-PS and brush were generated and processed through all pattern fabrication steps. In order to imitate the sidewall surface, a 32 nm thick X-PS film was prepared and subjected to the standard trim etch process. The trim etch process removes only 12 nm of the film, leaving a 20 nm thick oxygen-modified X-PS film, as illustrated in Figure 3a. All of the samples were subjected to the brush backfill process (coat, anneal, rinse) to simulate the full processing conditions prior to measurement of water contact angles.

The composition of the backfill brush (AZEMBLY^{TM} NLD-127, 51% PS) has been independently optimized at imec for 3x BCP DSA.[11] The surface coated with this brush (saturation thickness 7 nm) was measured to have a water contact angle (WCA) of 76.0°, roughly

halfway between the contact angles for PS (88.4°) and PMMA (63.2°). Surfaces with contact angles greater than the brush (more hydrophobic) are therefore expected to be more PS wetting; conversely, those with lower contact angles (more hydrophilic) are expected to be more PMMA wetting than the brush. The wetting behavior of the X-PS protected by photoresist during trim etch is not necessarily equivalent to that of the as-deposited material. In particular, treatment with solvents, resist, plasma, and other processing can modify the chemical nature of the stripes.[17] The WCA of the process-treated X-PS mimicking the protected guide stripe top was measured to be 83.7°, which is higher than the brush but lower than the as-deposited value of 88.4° due to chemical modification during processing. The top of the guide stripe is therefore weakly PS-preferential in wetting behavior. One of these modifications happens in the backfill step of the process; the brush not only grafts to a thickness of 7 nm in the bare wafer regions of the pattern but also grafts 1-2 nm on top of the X-PS. This thin additional layer partially screens the wetting nature of the underlying X-PS. In comparison, the WCA on the simulated sidewall was measured to be 73.3° after backfill processing, which is significantly higher than the WCA measured prior to backfill (53.2°) but still less than that of the saturated brush grafted to the substrate (76.0). The backfill treatment adds ~4 nm to the simulated sidewall, accounting for the change in contact angle during this process step. Since the water contact angle on this surface is lower than that of the backfill, it is expected to be preferentially wet by the PMMA domain of the BCP.

Water contact angle measurements are an indirect probe of surface energetics, however, and do not probe the full complexity of macromolecular surfaces. Therefore, to further demonstrate the wetting behavior of these surfaces, two lamellae-forming BCP thin films were annealed on large-

area surfaces representing the saturated brush, guide stripe top, and sidewall, respectively and their orientation on these substrates recorded (Figure 3c and d). Preferentially wetting surfaces direct lamellae to orient parallel to the substrate, leading to terraced holes or islands, whereas a range of weakly-preferentially wetting surfaces allow the lamellae to avoid terracing by adopting a perpendicular 'fingerprint' orientation.[18] The BCP orientation on a surface depends not only on the substrate chemistry but also on film thickness and BCP composition.[19, 20] Both BCP films formed fingerprint on the "backfill" (left column, Figure 3c and d), but they exhibited different wetting behavior on the other two surfaces. The first film, consisting of a symmetric BCP, showed PS-preferential wetting on the "guide stripe" but non-preferential wetting on the "sidewall." By contrast, the second film, consisting of a slightly PS-rich BCP, exhibited non-preferential wetting on the "guide stripe" but PMMA-preferential wetting on the "sidewall." The shift in wetting behavior can be understood by considering that a non-preferential surface for a slightly PS-rich BCP would be itself slightly PS-rich and therefore slightly PS-preferential for a symmetric BCP. These results indicate that the X-PS protected by the resist and the plasma-modified X-PS "sidewalls" after brush grafting and rinsing are weakly preferential for PS and PMMA, respectively.

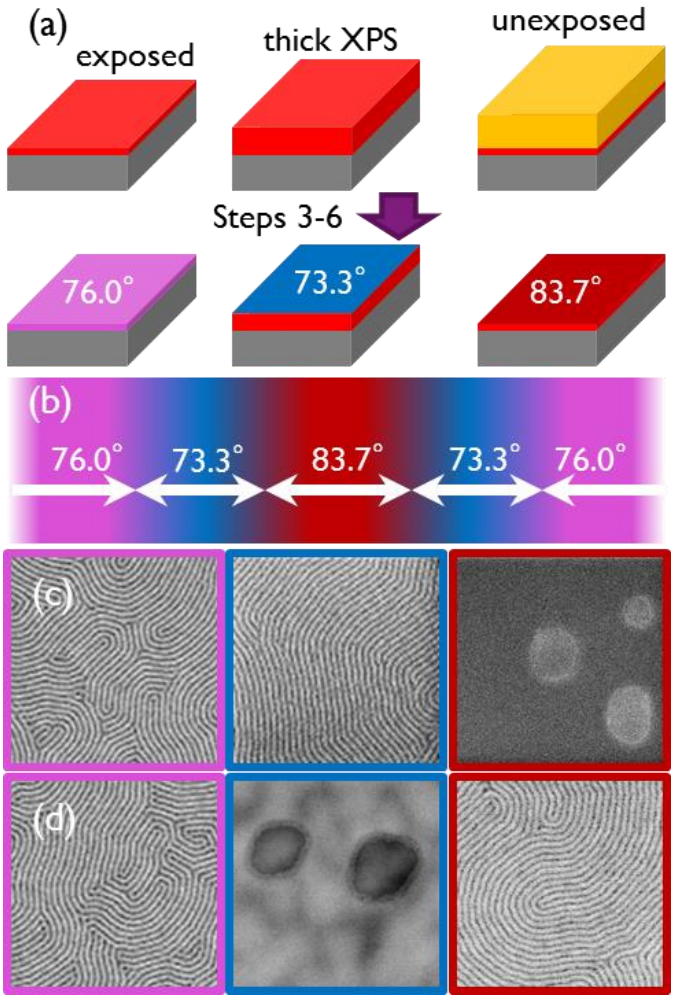

Figure 2-3. Unpatterned surfaces were processed with the steps described in Figure 1 to emulate the regions of the chemical pattern. The sidewall surface is simulated by etching partway through a thick coat of X-PS. Water contact angle measurements in (a) are associated with different regions of the chemical pattern, schematically illustrated from the top-down perspective in (b). Two BCP's were assembled on each surface in (c-d); the left, middle and right columns correspond to backfill, sidewall, and top surfaces, respectively. A symmetric BCP in (c) has PS-preferential wetting on the top of the guide stripe while a PS-rich lamellae-forming BCP in (d) has PMMA-preferential wetting on the sidewall. All other combinations resulted in perpendicular lamellae, indicative of non-preferential wetting.

BCP assembly on the chemical pattern is consistent with the three-tone description. This investigation focused on the use of 84 nm pitch chemical patterns and 28 nm L_0 block copolymer, for 3x density multiplication. When assembling the BCP on a series of chemical

patterns with different guide stripe widths, three ranges of guide stripe widths give ordered arrays. Representative images for each range of assembly are shown in Figure 4. Previous efforts in chemoepitaxial DSA have focused on using guide stripes roughly the width of one BCP domain, or half of the lamellar period.[12, 21] This regime of well-registered assembly is referred to as the "$0.5L_0$ window," where the PS-wetting guide stripe is nominally the width of one lamella, and can be observed in Figure 4(c). In this mode of registration, a PS domain (red) is centered over the guide stripe. The guide stripe is flanked by PMMA-wetting sidewalls with backfill brush in the interstitial space, resulting in a three-tone chemical pattern. A certain degree of incommensurability in the guide stripe width can be tolerated and still give good registration, but for guide stripes too narrow or too wide, the registration breaks down, as shown in Figure 4(b) and (d). Previous work has demonstrated the formation of complex non-bulk architectures on wider guide stripes ($W \sim L_0$) for which here we report fingerprint structures. The non-bulk morphologies form due to relatively strong preferential interactions with the guide stripe that dominate the polymer's natural tendency to adopt the lamellar configuration.[12, 13] Conversely, for a weakly interacting system where this substrate interaction is insufficient to overcome that tendency, one would expect the formation of undirected fingerprint. As discussed in the previous paragraph, our system is only weakly guiding in that all three regions of the pattern are within or near the range of non-preferential wetting conditions, leading to the fingerprint morphology observed in Figure 4(d).

For even wider guide stripes, where the stripe is roughly the width of three BCP domains, well-registered assembly is again observed as shown in Figure 4(e). This region of parameter space, known as the "$1.5L_0$ window," was also explored experimentally and through simulations

by Liu et al.[11] In this mode of registration, two PS domains separated by a PMMA domain lie over the guide stripe top. As shown in the first rows of Figure 2, the sidewalls of our widest guide stripes have the shallowest slopes (with angles below 15°). Sidewalls from adjacent guide stripes merge, leaving no area of SiN where the backfill brush grafts. Since these patterns only consist of protected X-PS guide stripes and plasma-modified X-PS sidewalls, they are two-tone in nature. The assembly on these structures exhibits a sort of symmetry, since two PS domains separated by a single PMMA domain form over the PS-preferential guide stripe, while two PMMA domains separated by a PS domain form over the PMMA-preferential sidewall. Even though top-down images of this mode of assembly show good registration, simulations presented in previous work indicate that when multiple domains wet the guide stripe, the 3D structure of the BCP domains can be quite complex.[11] Due to unfavorable enthalpic interactions with the pattern, the dissimilar domain over the center of each guiding region does not always extend through the film, and therefore these structures may not be suitable for pattern transfer.

In our system, a third mode of registration is also observed when the X-PS stripes are over-etched, to the point of leaving only the PMMA-wetting residual sidewall behind to guide the assembly. As illustrated in Figure 4a, these patterns also have a two-tone nature because they consist only of plasma-modified sidewall (preferential to PMMA) and backfill brush grafted to SiN. They are similar in design to the traditional $0.5L_0$ window in that only a single BCP domain is guided. In both this mode (denoted by the "residual assembly" window) and in the $1.5L_0$ mode, a PMMA domain is centered over the X-PS structure. Therefore, as the guide stripe width increases, the domain that is centered over the guide stripe transitions from PMMA-centered to PS-centered and then back to PMMA-centered. The fundamental change in centering mode is

evidenced by the breakdown in registration at guide stripe widths in the transition between windows of good assembly. The presence of a PMMA-preferential sidewall leads to a new assembly window, adds three-tone wetting in the standard $0.5L_0$ window, and composes the background for the $1.5L_0$ window.

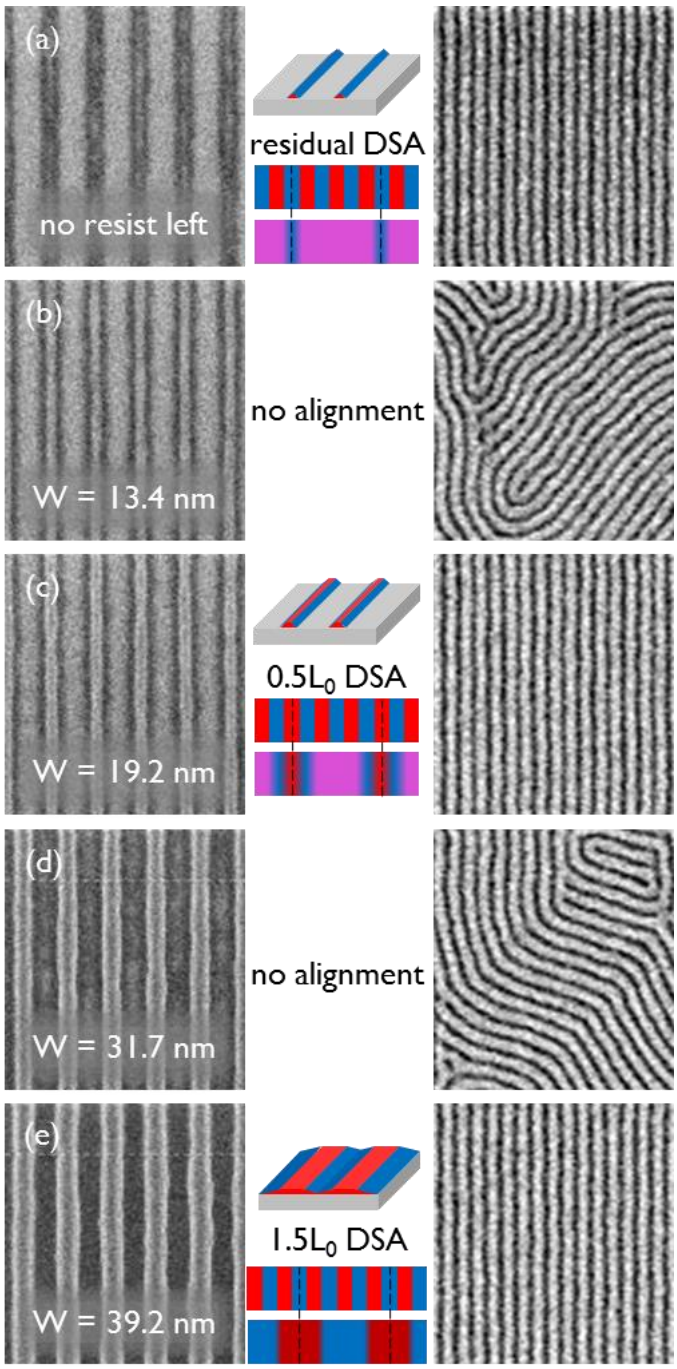

Figure 2-4. SEM images after trim etch and PMMA etch as W increases from (a) to (e). Three separate ranges (a), (c), and (e) lead to ordered arrays of BCP separated by ranges (b) and (d) corresponding to no pattern registration.

The evidence for the three-tone chemical pattern is further supplemented by experimental results when assembling a PS-rich BCP system that naturally forms PS microbridges, where PS domains connect through the PMMA domains, similar to a perforated lamellae morphology.[22, 23] As seen in Figure 5a, assembly of a PS-rich BCP on an unpatterned surface of 51% PS brush results in dense microbridges in all PMMA domains. When assembly takes place on a patterned surface, the microbridges still form over the brush. However, microbridge formation is suppressed over the PMMA-wetting sidewalls due to an enthalpically penalizing interaction between these surfaces and the PS microbridge structures. In the residual DSA regime (Figure 5b), every third PMMA domain is over a plasma-modified sidewall rather than the background and microbridges are confined to the other two-thirds of the PMMA domains over brush. In the $0.5L_0$ window (Figure 2-5c), a PS domain is over the guide stripe and two of the three PMMA domains assemble over the sidewall on either side. The third PMMA domain forms over the brush, and is therefore where microbridges are observed. For guide stripes in the $1.5L_0$ window (Figure 5d), adjacent sidewalls merge and no backfill brush region is present so microbridge formation is suppressed. In all cases, microbridge formation is observed primarily over the brush.

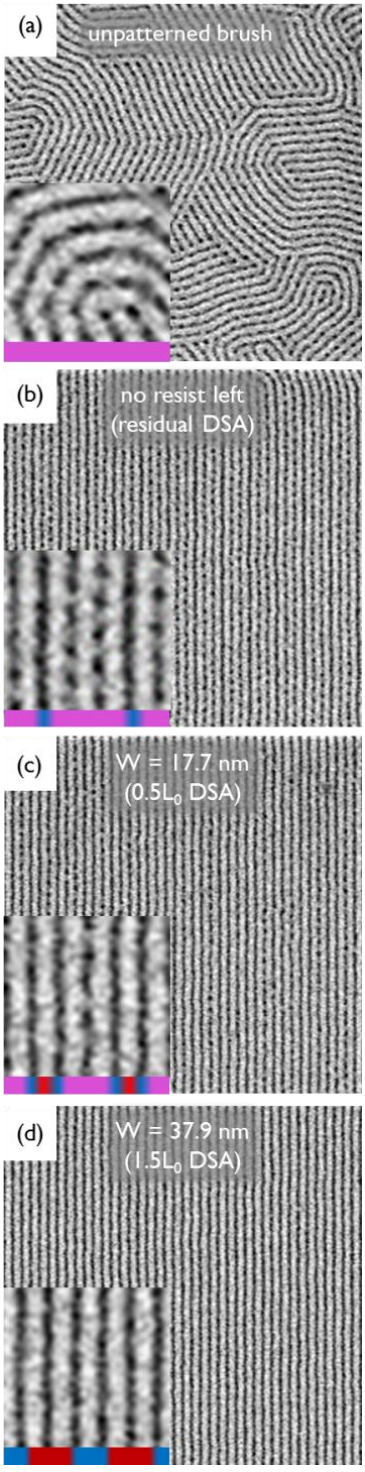

Figure 2-5. A BCP formulation that exhibits dense PS microbridges on (a) unpatterned brush, (b) overetched X-PS stripe, (c) guide stripe ~0.5 L_0, (d) guide stripe ~1.5L_0. In all cases, PS microbridges form over backfill brush rather than over plasma-treated X-PS sidewall.

The ideal substrate for chemoepitaxial DSA of through-film lamellar BCP with vertical sidewalls is the two-dimensional projection of the line-space array at its natural periodicity. Therefore, a one-to-one pattern with alternating PS and PMMA preferential stripes is best for assembly. The one-to-one pattern, however, does not provide any resolution enhancement for lithographic purposes. For applications requiring density multiplication, the target pattern consists of a sparse set of guide stripes of width $W = 0.5L_0$ preferential in wetting to one domain of the BCP while the background minimizes the interfacial energy with the remaining domains. In this case, the thermodynamic equilibrium structure is well-registered perpendicular lamellae, but the kinetics of assembly have been shown to be significantly slower than when one-to-one patterns are used.[16] Since three-tone patterns decouple the guiding nature of guide stripe, sidewall, and backfill, they can more closely resemble the two-dimensional projection of the desired BCP morphology. Specifically, in a traditional two-tone pattern with density multiplication, only one domain per guide stripe is directly guided by a preferential chemistry. The three-tone patterns potentially direct the assembly of three domains per patterned stripe: the domain over the guide stripe as well as the two adjacent domains over the sidewalls. In a fully optimized three-tone pattern, the geometry and chemistry of both guide stripe and sidewall would perfectly match those of their respectively guided BCP domains.

Furthermore, since DSA is a thermodynamically driven process, the free energy landscape dictates not only the equilibrium states but also the minimum free energy pathways along which the system evolves to the final assembled structure.[24] Past work has indicated that for some systems, registration defects may correspond to local energy minima, and that these states may therefore be kinetically trapped.[24, 25] For the system to bypass those states and reach the global

energy minimum and equilibrium morphology, it is necessary to reduce or eliminate energy barriers. In chemoepitaxy, the free energy landscape is a function of the boundary conditions imposed by the chemical pattern. Therefore, adding detail through the use of three-tone patterns can provide an avenue to modifying the system's free energy space, potentially resulting in fewer defects for a given annealing condition. Opportunities exist to better optimize materials and processes to realize more strongly preferential wetting three-tone patterns in the guiding feature and perhaps have even stronger positional control or accelerate defect annihilation.

In a recently published report, prepared concurrently with our study, Cushen et al.[8] describe a process comparable to our flow to direct the assembly of poly(trimethylsilylstyrene-*block*-*p*-methoxystyrene) (PTMSS-*b*-PMOST) with a topcoat. They used e-beam lithography and plasma etch to pattern stripes in an 8 nm thick X-PS. A 3 nm thick PS brush was used to backfill the pattern. In their system, Cushen et al. consider the photoresist-protected stripe and brush to be non-preferential to both blocks. The guiding features for the pattern are reported to be the sidewalls of the trim etched X-PS that rise is 5 nm above the thickness of the backfill. They assembled the BCP through thermal annealing with a non-preferential top coat. In this manner, they succeeded in making a 'double-patterned' substrate that combines graphoepitaxy with chemoepitaxy to guide two domains per lithographically defined line. These patterns are similar to the ones used in our work in that they both use a plasma treatment that modifies the sidewall, causing it to be preferentially wetting by one of the domains, and are made using the same general process flow. A key attribute of the chemical patterns reported here and by Cushen et al. is that the region of the patterns defined by the sidewalls are at twice the density of features of the photoresist features originally patterned in the lithography process.

2-5. Conclusions

We have identified a method to make a new style of chemical pattern and characterized the geometry and wetting behavior of its components. Certain processing conditions result in chemical patterns with three regions of distinct wetting behavior: PS-preferential guide stripes, PMMA-wetting sidewalls, and weakly-preferential background. Evidence of three-tone patterns was supported by certain BCP DSA behavior that cannot be explained by a two-tone description of the chemical pattern. For chemoepitaxial density multiplication, a three-tone chemical pattern directs assembly with three times the number of guided domains and therefore is an avenue for increased control of the assembly behavior. The creation of three-tone patterns described here pertains strictly to the exact materials, tools, and processing conditions of the DSA line at imec. Future improvement of chemical pattern processing should account for and optimize the properties of the sidewall to achieve the highest quality of DSA for these three-tone patterns.

Whereas our discussion has focused on the creation of three-tone chemical patterns, the concept of innovation in processing to improve patterns for DSA is more broadly applicable. Past work has focused on novel material development as the primary driver for enhanced performance, but here we have demonstrated how creative development in processing could play a key role. Knowledge of fundamental science behind DSA will enable continued innovation in materials and processing.

2-6 References

1. ITRS *Lithography*; 2013.

2. Bates, F. S.; Fredrickson, G. H. *Physics Today* **1999,** 52, (2), 32-38.

3. Ruiz, R.; Kang, H.; Detcheverry, F. A.; Dobisz, E.; Kercher, D. S.; Albrecht, T. R.; de Pablo, J. J.; Nealey, P. F. *Science* **2008,** 321, (5891), 936-939.

4. Kim, S. O.; Solak, H. H.; Stoykovich, M. P.; Ferrier, N. J.; de Pablo, J. J.; Nealey, P. F. *Nature* **2003,** 424, (6947), 411-414.

5. Cheng, J. Y.; Sanders, D. P.; Truong, H. D.; Harrer, S.; Friz, A.; Holmes, S.; Colburn, M.; Hinsberg, W. D. *Acs Nano* **2010,** 4, (8), 4815-4823.

6. Bencher, C.; Finders, J.; Englard, I.; Cohen, Y.; Sagiv, A.; Ben-Yishai, M.; Mangan, S.; Dai, H.; Ngai, C.; Dotan, K.; Knops, R.; Mouraille, O.; Mos, E.; Kremer, A. *Journal of Micro-Nanolithography Mems and Moems* **2011,** 10, (4).

7. Kim, J.; Yin, J.; Cao, Y.; Her, Y.; Petermann, C.; Wu, H.; Shan, J.; Tsutsumi, T.; Lin, G. *Proc. SPIE Advanced Lithography* **2015,** 9423, 94230R.

8. Cushen, J.; Wan, L.; Blachut, G.; Maher, M. J.; Albrecht, T. R.; Ellison, C. J.; Willson, C. G.; Ruiz, R. *ACS Applied Materials & Interfaces* **2015,** 7, (24), 13476-13483.

9. Edwards, E. W.; Montague, M. F.; Solak, H. H.; Hawker, C. J.; Nealey, P. F. *Advanced Materials* **2004,** 16, (15), 1315-1319.

10. Edwards, E. W.; Mueller, M.; Stoykovich, M. P.; Solak, H. H.; de Pablo, J. J.; Nealey, P. F. *Macromolecules* **2007,** 40, (1), 90-96.

11. Liu, C.-C.; Ramirez-Hernandez, A.; Han, E.; Craig, G. S. W.; Tada, Y.; Yoshida, H.; Kang, H.; Ji, S.; Gopalan, P.; de Pablo, J. J.; Nealey, P. F. *Macromolecules* **2013,** 46, (4), 1415-1424.

12. Liu, C.-C.; Han, E.; Onses, M. S.; Thode, C. J.; Ji, S.; Gopalan, P.; Nealey, P. F. *Macromolecules* **2011,** 44, (7), 1876-1885.

13. Khaira, G. S.; Qin, J.; Garner, G. P.; Xiong, S.; Wan, L.; Ruiz, R.; Jaeger, H. M.; Nealey, P. F.; de Pablo, J. J. *Acs Macro Letters* **2014,** 3, (8), 747-752.

14. Kim, S.; Nealey, P. F.; Bates, F. S. *Nano Letters* **2014,** 14, (1), 148-152.

15. Delgadillo, P. A. R.; Gronheid, R.; Thode, C. J.; Wu, H.; Cao, Y.; Neisser, M.; Somervell, M.; Nafus, K.; Nealey, P. F. *Journal of Micro-Nanolithography Mems and Moems* **2012,** 11, (3).

16. Liu, G.; Delcambre, S. P.; Stuen, K. O.; Craig, G. S. W.; De Pablo, J. J.; Nealey, P. F.; Nygard, K.; Satapathy, D. K.; Bunk, O.; Solak, H. H. *Journal of Vacuum Science & Technology B* **2010,** 28, (6), C6B13-C6B19.

17. Williamson, L.; Lin, G.; Cao, Y.; Gronheid, R.; Nealey, P. *SPIE Advanced Lithography* **2014,** 9049, 9049-1B.

18. Fasolka, M. J.; Mayes, A. M. *Ann. Rev. Mater. Res.* **2001,** 31, 323-355.

19. Suh, H. S.; Kang, H.; Nealey, P. F.; Char, K. *Macromolecules* **2010,** 43, (10), 4744-4751.

20. Han, E.; Stuen, K. O.; La, Y.-H.; Nealey, P. F.; Gopalan, P. *Macromolecules* **2008,** 41, (23), 9090-9097.

21. Detcheverry, F. A.; Liu, G.; Nealey, P. F.; de Pablo, J. J. *Macromolecules* **2010,** 43, (7), 3446-3454.

22. Khandpur, A. K.; Forster, S.; Bates, F. S.; Hamley, I. W.; Ryan, A. J.; Bras, W.; Almdal, K.; Mortensen, K. *Macromolecules* **1995,** 28, (26), 8796-8806.

23. Perego, M.; Ferrarese Lupi, F.; Ceresoli, M.; Giammaria, T. J.; Seguini, G.; Enrico, E.; Boarino, L.; Antonioli, D.; Gianotti, V.; Sparnacci, K.; Laus, M. *Journal of Materials Chemistry C* **2014,** 2, (32), 6655-6664.

24. Li, W.; Nealey, P. F.; de Pablo, J. J.; Mueller, M. *Physical Review Letters* **2014,** 113, (16), 8301-8301.

25. Mueller, M.; de Pablo, J. J. *Annual Review of Materials Research, Vol 43* **2013,** 43, 1-34.

Chapter 3:

Influence of Guide Stripe Composition on DSA

3-1 Abstract

Chemoepitaxial directed self-assembly (DSA) of block copolymer (BCP) films uses chemical patterns composed of guide stripes and background regions to align BCP lamellar domains. The wetting behaviors of the guide stripe and background regions in the chemical pattern are fundamental parameters for chemoepitaxial DSA. Guide stripes were made from a series of four cross-linkable polystyrene-rich materials and the kinetics of block copolymer assembly on the resulting chemical patterns were evaluated by assessing the DSA quality through a range of guide stripe widths and pitches. The range of commensurability tolerance increased through both guide stripe width and pitch for higher polystyrene content in the guide stripe and longer anneal time. However, when the degree of partial alignment for patterns made from each guide stripe material is considered, the ultimate thermodynamic commensurability tolerance can be extrapolated from the kinetics study and is independent of anneal time. The DSA performance was also evaluated based on line edge roughness, which increased as the guide stripe became less preferential.

3-2 Introduction

Block copolymer directed self-assembly (BCP DSA) is a promising resolution enhancement technique for dense arrays of features, where naturally forming microdomains are aligned through a thermodynamically driven process.[1-2] In chemoepitaxial DSA, the substrate is composed of chemically distinct regions that are designed to interact with the BCP to induce

long-range order. A lithographic template can be used to define sparse guide stripes for a chemical pattern, where one of the BCP phases preferentially wets the guide stripes and the remaining domains assemble over the background region.[3] The best surfaces to use in a chemical pattern minimize the interfacial energy between the pattern and the BCP in the aligned state. Since the backfill region is designed to be in contact with both domains, the optimum backfill can be achieved by selecting the proper backfill material that minimizes the interfacial energy with the BCP domains that it contacts, as described by Liu et al.[4] The optimum guide stripe material (GSM) only needs to minimize the interfacial energy with the guided domain by matching the chemistry of the guide stripe with the guided domain, similar to the design of chemical patterns with no resolution enhancement. The total interfacial energy between the BCP and chemical pattern is minimized when the BCP is perfectly registered, which is the driving force for chemoepitaxial DSA. The aligned system gains an enthalpic benefit compared to randomly oriented vertical lamellae, but that alignment imparts an entropic penalty due to restricting the BCP domains. The equilibrium structure favors aligned domains when the enthalpic benefit exceeds the entropic penalty for alignment. This balance between enthalpy and entropy was developed by Edwards et al. for the case where the resolution of the chemical pattern is matched to that of the assembled BCP.[5]

In this study, poly(styrene-*block*-methyl methacrylate) (PS-*b*-PMMA) BCP was assembled on chemical patterns that were generated from a series of PS-rich cross-linkable random copolymer P(S-*r*-MMA) guide stripe materials. Higher polystyrene content is associated with more preferential wetting of the PS block, leading to larger geometric commensurability tolerance (guide stripe width and pitch) for assembly at a given annealing condition. This trend was more

noticeable at short annealing time when the DSA is partially aligned on slightly incommensurate patterns; at longer anneal times, the geometric commensurability converges on the same thermodynamic tolerance for all guide stripe compositions. Furthermore, the line edge roughness (LER) of the DSA pattern is reduced by using a strongly preferential guide stripe composition.

3-3 Experimental Section

A. Materials

A series of cross-linkable P(S-*r*-MMA) guide stripe materials (AZEMBLY^{TM} NLD-300, NLD-301, NLD-302, and NLD-128), P(S-*r*-MMA) brush (AZEMBLY^{TM} NLD-127), and P(S-*b*-MMA) BCP (AZEMBLY^{TM} PME-312) were provided by Merck Performance Materials. ArF photoresist AIM5484 was purchased from JSR Micro. Orgasolv® STR 301 was purchased from BASF. RER600 was purchased from Fujifilm.

B. DSA process

Sample processing was performed on imec's 300 mm process line in Belgium as described previously.[6] A 13 nm film of silicon nitride was deposited on 300 mm Si wafers for reflectivity control. An 8 nm film of cross-linkable guide stripe material was spincast, then annealed at 315°C for 5 min in a nitrogen environment using a TEL ACT12 track. AIM5484 was spincast (95 nm) using a SOKUDO DUO track, exposed on an ASML 1950 immersion scanner (optimum dose = 13 mJ, optimum focus = -0.02 μm, NA = 1.35, dipole illumination $\sigma_o = 0.87$ $\sigma_o = 0.76$, blade angle = 40°), then developed using manufacturer recommended settings. The resist and X-PS were trim etched in a Lam plasma etch chamber. The remaining resist was stripped with Orgasolv in a TEL ACT12 track. The pattern was backfilled by coating 50 nm of AZEMBLY^{TM} NLD-127, then annealing for 5 min at 250°C, resulting in 7 nm of brush grafted to the bare

regions of underlying substrate. The wafer was rinsed with RER600 to remove ungrafted brush and dried with a 100°C, 1 min bake. BCP was spincoated onto a chemical pattern at 1500 RPM, soft baked at 100°C for 1 min to remove solvent, and then annealed at 250°C for 1, 5, or 240 min. PMMA was etched on the TEL TACTRAS plasma etch chamber for enhanced imaging contrast.

C. Characterization:

Scanning electron microscope (SEM) imaging was performed with a Hitachi CG5000 after trim etch and after PMMA domain removal. The line width (W) of the photoresist structures after trim etch was measured by automated built-in Hitachi software. Static water contact angle measurements were obtained using a Dataphysics OCAH230L contact angle measurement system. A syringe dispensed 5 μL drops of deionized water, which were measured after 0.3 s of stabilization. Line edge roughness was measured using LERDEMO version 2014b software on rectangular scan (0.45μm x 2.25μm) SEM images taken with a Hitachi CG5000.

3-4 Results and Discussion

Chemical patterns were generated using a series of poly(styrene-*random*-polymethyl metacrylate) P(S-*r*-MMA) guide stripe materials (GSM) at step 1 of Figure 3-1 in order to align the lamellae-forming block copolymer (BCP). This layer is fabricated into guide stripes by patterning photoresist with immersion lithography, and then trimming the photoresist lines with plasma etching. The remaining resist is stripped and a random copolymer brush is grafted to the uncovered substrate between the guide stripes. A BCP film is coated and annealed on the resulting chemical pattern and the PMMA domain is selectively removed with plasma etching, resulting in a line-space array with 3x pitch reduction compared to the initial patterned resist.

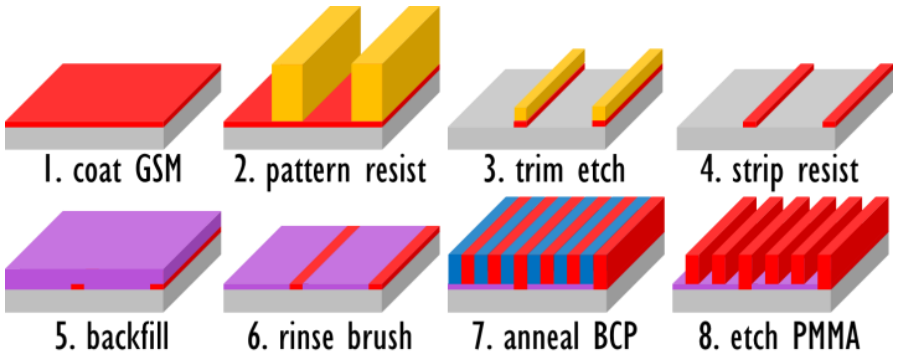

Figure 3-1. Schematic of process flow for fabricating the chemical patterns and assembling BCP

The wetting behavior for all guide stripe materials was determined on a large-area unexposed surface as a function of composition after processing. The GSM differ in composition from 80-100% PS, but all of them were modified to be less PS-preferential than the as-cast material by the chemical pattern fabrication process, specifically by the trim etch and backfill steps.[7] The water contact angle of the GSM in the final chemical pattern ranges from 83.7° to 79.4° as the PS content decreases as seen in Figure 3-2. Lower water contact angles indicate a more polar and thus less PS-preferential surface, both from GSM composition and process modification. All of these surfaces are more hydrophobic than the backfill brush (contact angle of 76.0°) indicating that the guide stripes are always more PS-preferential than the background region. Note that WCA probes the very top surface, whereas polymers can form a thicker interpenetrated interface; in the context of this study, the brush grafted to the GSM may over-represent the modification. However, BCP annealed on each of the simulated guide stripe surfaces assembles as vertical fingerprint lamellae, indicating that none of the surfaces are strongly selective to the PS block.

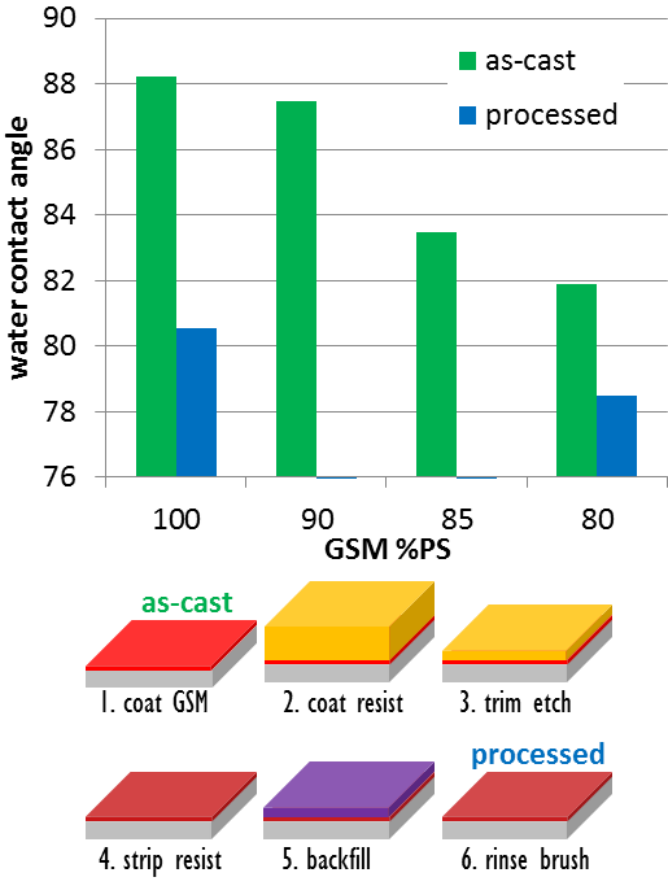

Figure 3-2. Water contact angle of each GSM before and after processing to simulate the guide stripe surface. Lower water contact angles correspond to less PS-preferential surfaces.

BCP films were assembled on patterns with a series of pattern fields with a range of guide stripe pitches and widths generated from each of the four GSM. The range of conditions that are well-aligned was assessed after the BCP was annealed for 1 min at 250 °C by inspecting a single SEM image with 2.75 x 2.75 μm field of view for each field, then assigning it as defect-free (green) or containing misalignment (red) in Figure 3. The data are fit with an axis-aligned ellipse by balancing the number of good and bad fields that are on the wrong side of the ellipse boundary. The dimensions of the ellipses quantify the geometric commensurability window for a given wafer as a metric to evaluate the DSA performance through different guide stripes. Note

that the pitch of the guide stripes, L_S, is normalized by the natural periodicity of the BCP (L_0 = 28 nm). Also, the width of the guide stripes, W, has been normalized to the lamellar period imposed by the pattern, $L_S/3$, which can be different from L_0. This normalization minimizes the covariance of the commensurability ellipses that would otherwise be present without proper normalization, meaning that all L_S have the same optimal normalized W. The major and minor axes of the commensurability ellipse correspond to the maximum guide stripe width and pitch commensurability tolerances, respectively. Both geometric parameters impose an entropic penalty for DSA and are therefore correlated from sample to sample.

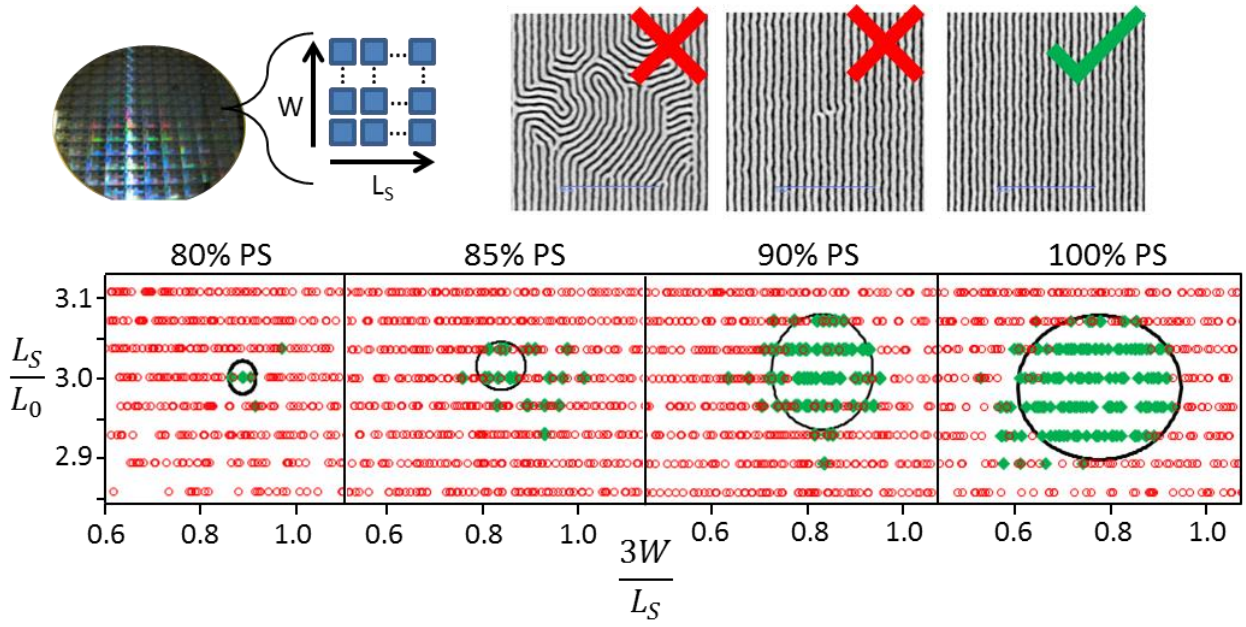

	80%PS	85%PS	90%PS	100%PS
trim	0.028	0.051	0.11	0.17
pitch	0.021	0.030	0.072	0.090

Figure 3-3. Geometric commensurability is assessed for different guide stripe compositions after 1 min of anneal. Fields with perfect registration in the representative field of view are marked green. An axis-aligned ellipse is fit to the data to describe the range of guide stripe width and pitch commensurability. The range of commensurability in width and pitch are the major and minor axes of the ellipse.

A more detailed analysis of these SEM images measures the degree of alignment after DSA, leading to more information at the edge of the commensurability window. A custom image analysis algorithm vertically smears the image in-line with the pattern stripes so that misaligned regions are blurred and thus detected. An example of the misalignment identified in this manner is shaded red in Figure 3-4a. As the chemical pattern is increasingly non-optimal, the area fraction of misalignment linearly increases. At a certain threshold, the BCP is randomly aligned and saturates at a value of ~0.8 for an unguided system for this analysis because some regions will statistically be in the direction of interest. The fraction of misalignment is plotted through guide stripe width in Figure 4b. To avoid congestion in the figure, only two series of misalignment measurements are plotted; the omitted misalignment cross-sections are included in the supplemental material. A linear regression is plotted through the misalignment fraction for narrow guide stripe widths and the slope of the regression is plotted for all four GSM at two pitches in Figure 3-4c. GSM with higher PS content have a sharper transition between perfect registration and no alignment.

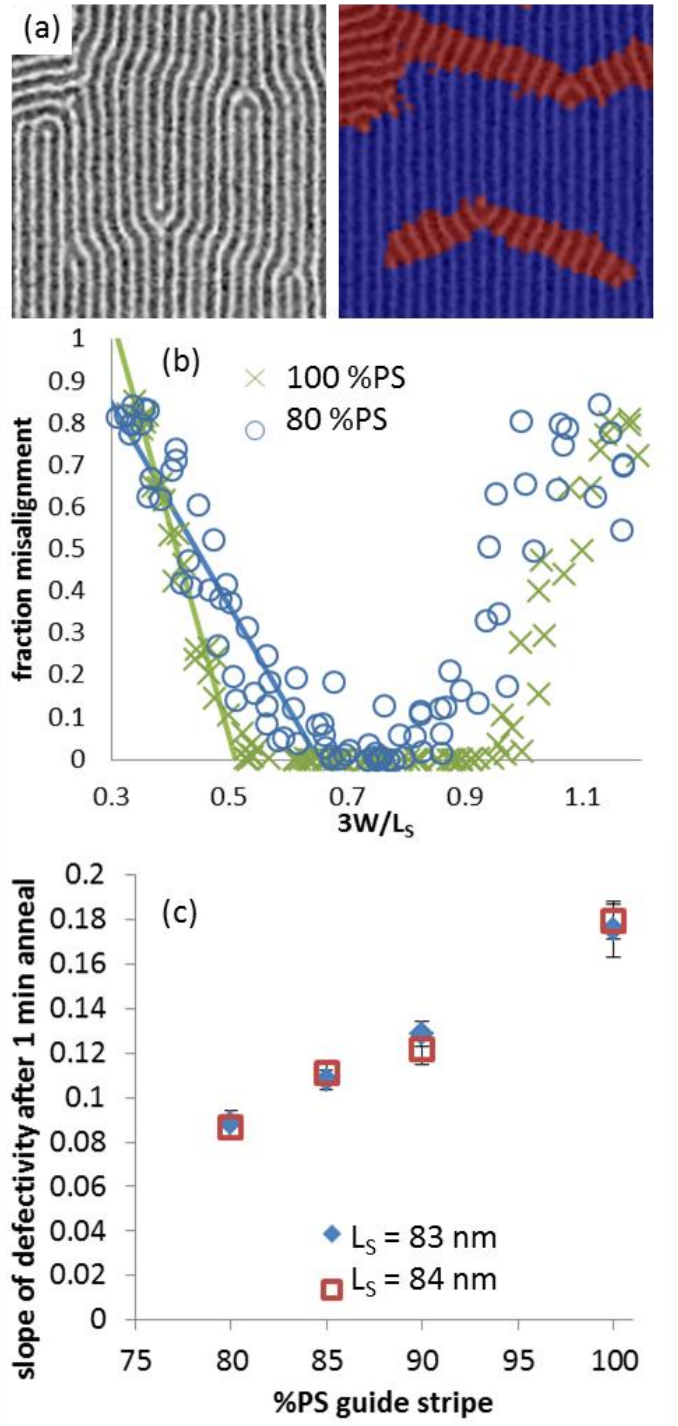

Figure 3-4. (a) Sample image with 20% fraction misalignment marking the aligned BCP in blue and misaligned BCP in red. (b) The fraction of misalignment through guide stripe width at optimum pitch. (c) The gradient in the misalignment area for the series of GSM. A steeper transition to the ordered regime is observed for a more preferential guide stripe (higher %PS).

Additional annealing of the BCP on chemical patterns increased the commensurability window. Notably, the pitch and guide stripe width tolerance increases dramatically from 1 min to 5 min of annealing, and the commensurability tolerances for different GSM converge. Annealing for 4 hr has little effect on the commensurability tolerance, suggesting that it approaches a maximum range. Further evidence for the presence of a maximum geometric tolerance for a given system is illustrated by the area fraction of misalignment plotted through the guide stripe width in Figure 3-5b. The gradient in misalignment fraction is steeper at longer anneal time, but the boundaries of the process window with completely random orientation are unchanged. This boundary defines the maximum commensurability window independent of anneal time and is identifiable after a 1 min anneal. Previous work has demonstrated that ultimate defect density at the best pattern geometry continues to improve with long anneal times, which is beyond the sensitivity of this analysis.[8]

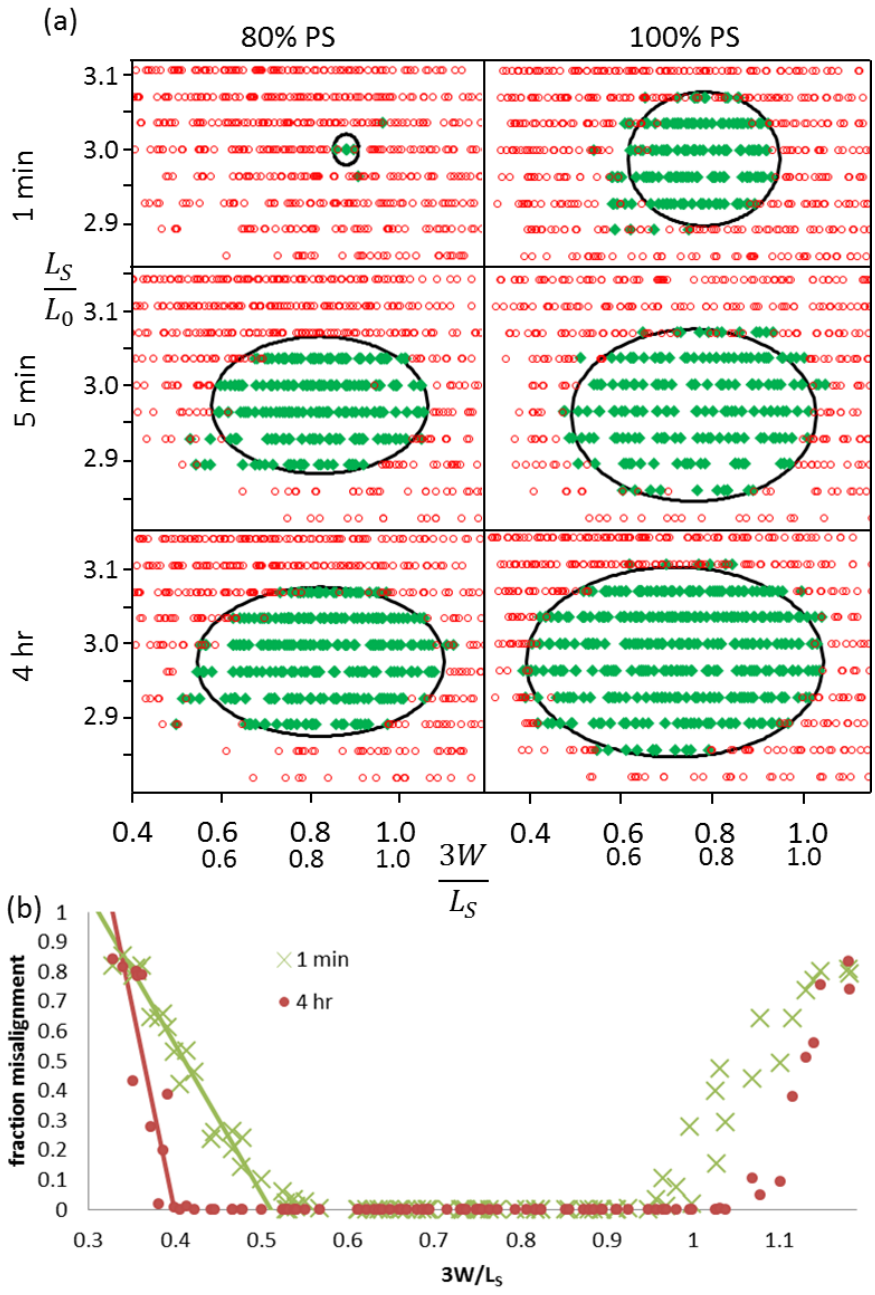

Figure 3-5. (a) Geometric commensurability after 1, 5 min and 4 hr BCP anneal. (b) Fraction of misalignment for 100% PS GSM after 1 min and 4 hr BCP anneal. Additional annealing increases the number of defect-free fields, but does not alter the maximum commensurability tolerance.

In addition to misalignment defects, line edge roughness (LER) is also sensitive to the free energy balance of the DSA system. The LER of the BCP domains was measured in the field of optimal pattern dimensions after PMMA removal. As the guide stripe wetting selectivity decreases, the LER increases as demonstrated in Figure 3-6. The trend in LER demonstrates that a stronger thermodynamic interaction between the guide stripe and guided domain corresponds to tighter control over the placement of the BCP domains and therefore lower LER.

Line edge roughness is associated with the tendency of the polymer domain to introduce spontaneous curvature. Entropically, the polymer would prefer to assemble with spontaneous curvature, as found in an unguided system. This tendency to induce curvature generates local variation in the line placement for a guided system. The higher the enthalpic driving force, the more that the entropic effects can be overcome, resulting in lower LER.

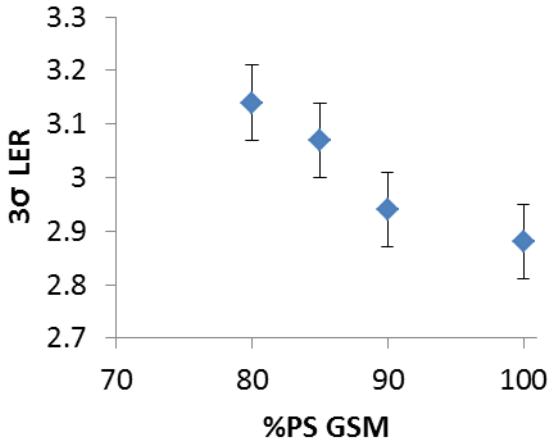

Figure 3-6. Line edge roughness comparing DSA performance on the series of GSM.

All non-idealities in the DSA system are sources of penalties in the driving force for achieving pattern registration. The primary parameters for chemical pattern design are the guide stripe and backfill materials, and the pitch and width of the guide stripes. The chemistry of the chemical pattern regions determines the interfacial energy between the pattern surfaces and the BCP domains. The interfacial energies dictate the enthalpic benefit for the BCP to epitaxially align to the guide stripes. In contrast, the geometric incommensurability exacerbates the entropic penalty when polymer chains are required to adopt conformations deviating from the unguided polymer behavior, which can slow or prevent pattern registration.

The system is most sensitive to differences in driving force for DSA at short anneal times, so identifying the system parameters with the strongest driving force is most straight-forward at short annealing times. The driving force for assembly is independent of anneal time, and a pattern that gives better assembly at short anneal times is expected to always have the best defectivity for a given BCP anneal. For a given anneal time, a larger commensurability tolerance indicates that the chemical pattern provides a higher enthalpic gain for DSA, as it is able to overcome a larger entropic penalty. The simple SEM image analysis approach to identify the degree of registration is only sensitive to partially aligned systems, but the registration at a short anneal time could be correlated with vanishing defect density for an equivalent system given a longer anneal.

3-5 Conclusion

This work demonstrates the importance of the preferential wetting nature of the guide stripe in a chemical pattern for BCP DSA. Any reduction in the guide stripe wetting selectivity should be minimized in order to achieve the best DSA performance, both through defectivity and LER

metrics. A stronger guide stripe contributes a larger enthalpic gain for alignment, increasing the pitch commensurability and decreasing line edge roughness. It is not clear whether a guide stripe can be more selective in wetting of one block than a guide stripe of matching polymer chemistry. However, any modification that reduces the wetting selectivity decreases the driving force for DSA. Such a modification impedes defect annihilation and contributes to line edge roughness in the assembled domains.

3-6 References

1. Cheng, J. Y.; Rettner, C. T.; Sanders, D. P.; Kim, H. C.; Hinsberg, W. D. *Adv. Mater* **2008**, 20, 3155-3158.

2. Detcheverry, F. A.; Liu, G.; Nealey, P. F.; de Pablo, J. J. *Macromolecules* **2010**, 43, (7), 3446-3454.

3. Liu, C. C.; Han, E.; Onses, M. S.; Thode, C. J.; Ji, S.; Gopalan, P.; Nealey, P. F. *Macromolecules* **2011**, 44, 1876-1885.

4. Liu, C.-C.; Ramirez-Hernandez, A.; Han, E.; Craig, G. S. W.; Tada, Y.; Yoshida, H.; Kang, H.; Ji, S.; Gopalan, P.; de Pablo, J. J.; Nealey, P. F. *Macromolecules* **2013,** 46, (4), 1415-1424.

5. Edwards, E. W.; Montague, M. F.; Solak, H. H.; Hawker, C. J.; Nealey, P. F. *Advanced Materials* **2004,** 16, (15), 1315-1319.

6. Liu, C.-C.; Thode, C. J.; Delgadillo, P. A. R.; Craig, G. S. W.; Nealey, P. F.; Gronheid, R. *J. of Vac. Sci. Technol. B* **2011,** 29(6) 06F203-1.

7. Williamson, L., Lin, G.; Cao, Y.; Gronheid, R.; Nealey, P.F. *SPIE Advanced Lithography* **2014,** 9049, 9049-1B.

8. Delgadillo, P. A. R.; Harukawa, R.; Parnell, D.; Lee, Y.-T.; Chan, B. T.; Lin, G.; Cao, Y.; Nagaswami, V. R.; Somervell, M. H.; Nafus, K.; Gronheid, R.; Nealey, P. F. *SPIE Advanced Lithography* **2014,** 9049, 9049-19.

Chapter 4:

Impact of BCP Asymmetry on DSA Patterning Performance

4-1 Abstract

Reduction of defects in block copolymer directed self-assembly (BCP DSA) remains the primary limitation for its implementation in high-volume semiconductor manufacturing. Progress to date demonstrates encouraging results, but the source and impact of non-idealities in the system need to be assessed and corrected. When an asymmetric lamellae-forming BCP is assembled on chemical patterns, the patterning performance and defect modes change depending on whether the majority or minority volume fraction phase is guided by the chemical pattern. Asymmetric BCP formulations were generated by blending homopolymer with a symmetric BCP. The patterning performance of the BCP formulations was assessed for different pattern pitches, guide stripe widths, backfill materials, and annealing times. Optical defect inspection and SEM review were used to track the defect modes for each formulation. Formulation-dependent trends in defect modes show the importance of optimizing the BCP formulation in order to minimize the defectivity.

4-2 Introduction

Lamellae-forming block copolymers (BCP) are being investigated for generating dense line arrays through directed self-assembly (DSA) as a multi-patterning enhancement of advanced photolithography. One avenue to BCP DSA uses a chemical pattern composed of guide stripes that are preferentially wet by one block in a background that is weakly preferential to the opposite block in order to generate an aligned array over macroscopic dimensions. However, the

array can contain defects associated with the self-assembly process. Previous work has addressed pattern design to minimize defects, but the BCP characteristics must also be optimized to meet defect density requirements.

Many defect modes can disrupt the pattern performance in DSA. Some defects are common among all lithography approaches including embedded or fall-on particles, which are associated with system cleanliness whereas pattern collapse is related to the mechanical properties of the features. Line breaks or bridges are also traditional defects, but DSA introduces a new mechanism for them through non-bulk BCP structures. Misregistration of self-assembled features such as dislocation pairs is a unique defect mode for DSA techniques and will be the focus in this work. Misregistration defects have been calculated to be highly unfavorable thermodynamically[1], but macromolecular assembly can be kinetically limited as it moves toward the thermodynamic minimum.[2] Many aspects contribute to the driving force for the system to equilibrate, such as the interfacial energy between the pattern surfaces and the BCP and the pattern commensurability to the natural periodicity. A higher enthalpic gain for the BCP to align to the chemical pattern manifests as faster assembly kinetics on perfectly commensurate patterns as well as a larger tolerance for the entropic penalty of stretching or compressing the domain spacing.

BCP formulations with symmetric volume fraction of the blocks are typically used to study lamellae. However, the lamellar morphology is thermodynamically stable for BCP systems +/- 10% volume fraction from symmetry.[3] The overall volume fraction of the BCP formulation can be tuned by adding small amount of homopolymer (HP), as demonstrated by Campbell et al. For

unguided perpendicular lamellae, the domain connectivity changes to favor the majority domain, regardless of which domain is in excess.[4]

This study examines the role of asymmetry in a poly(styrene-*block*-methyl methacrylate) (PS-*b*-PMMA) BCP using chemoepitaxial DSA. Whereas the unguided morphology behavior is symmetric with volume fraction, the chemical pattern breaks this symmetry, as one block is preferentially wet by the guide stripes to guide the assembly behavior. The patterning performance of a given set of process conditions is assessed in this work by the range of pattern geometries (pitch and guide stripe width) in order to amplify the misregistration defect mode. In this work, we demonstrate that a PS-guided chemical pattern leads to asymmetric DSA performance through BCP volume fraction. PMMA-rich formulations assemble over a smaller geometric commensurability tolerance and are prone to disclination-style misregistration defects, whereas PS-rich formulations have a large range of pattern commensurability tolerance but generate microbridge defects observed after pattern transfer.

4-3 Experimental Section

A. Materials

Cross-linkable polystyrene (AZEMBLY^{TM} NLD-128), P(S-*r*-MMA) brushes (AZEMBLY^{TM} NLD-127 and NLD-208A-D), P(S-*b*-MMA) BCP (AZEMBLY^{TM} PME-673 and PME-674) and PS and PMMA homopolymers (AZEMBLY^{TM} PME-675 and PME-676) were provided by Merck Performance Materials. ArF photoresist AIM5484 was purchased from JSR Micro. Orgasolv® STR 301 was purchased from BASF. Propylene glycol methyl ether acetate (PGMEA) was purchased from Fujifilm.

B. Chemical pattern fabrication

The chemical patterns were fabricated at imec as described previously.[5] A 13 nm film of silicon nitride was deposited on 300 mm Si wafers using PECVD at 480°C for antireflectivity and hardmask applications. An 8 nm film of X-PS was spincast, then annealed at 315°C for 5 min in a nitrogen environment using a TEL ACT12 track. AIM5484 was coated (95 nm) using a SOKUDO DUO track, exposed on ASML 1950 immersion scanner (optimum dose = 11 mJ, optimum focus = -0.02 μm, NA = 1.35, dipole illumination $\sigma_o = 0.98$ $\sigma_o = 0.86$, blade angle = 40°) then developed using manufacturer recommended settings. The resist and X-PS were trim etched in a Lam plasma etch chamber. The remaining resist was stripped with Orgasolv in a TEL ACT12 track. The pattern was backfilled by coating 50 nm of NLD-127, then annealing for 5 min at 250°C, resulting in 7 nm of brush grafted to the bare regions of the underlying substrate. The wafer was rinsed with PGMEA to remove ungrafted brush and dried with a 100°C, 1 min bake.

C. Block copolymer processing

Solutions of pure BCP and HP of equal concentration in PGMEA were mixed to create formulations with a series of volume fractions. Each formulation was spincoated onto a chemical pattern at 1500 RPM, soft baked at 100°C for 1 min to remove solvent, then annealed at 250°C for 1, 5 or 240 min. PMMA was etched on the TEL TACTRAS plasma etch chamber. The remaining PS pattern was then transferred into the silicon through a series of etch steps in the TEL TACTRAS.

D. Characterization

SEM imaging was performed on a Hitachi CG4000 or CG5000 after trim etch, PMMA removal, and pattern transfer. The guide stripe widths, W, were determined by measuring the linewidth of the resist remaining after trim etch using Hitachi's in-line analysis. Defect detection was accomplished on KLA 2835 and defects were SEM reviewed on KLA eDR 7100. Defect classification was assessed manually.

4-4 RESULTS AND DISCUSSION

Small amounts of polystyrene (PS) or poly(methyl methacrylate) (PMMA) homopolymer (HP) were blended into a symmetric PS-*b*-PMMA block copolymer (BCP) to adjust the overall volume fraction of the formulation.[4] Addition of homopolymer also increases the domain spacing of the blend, L_B, as shown in Figure 4-1. The HP has a molecular weight comparable to the corresponding block and therefore swells the corresponding domain according to the dry brush regime and localizes in the middle of the domain.[6]

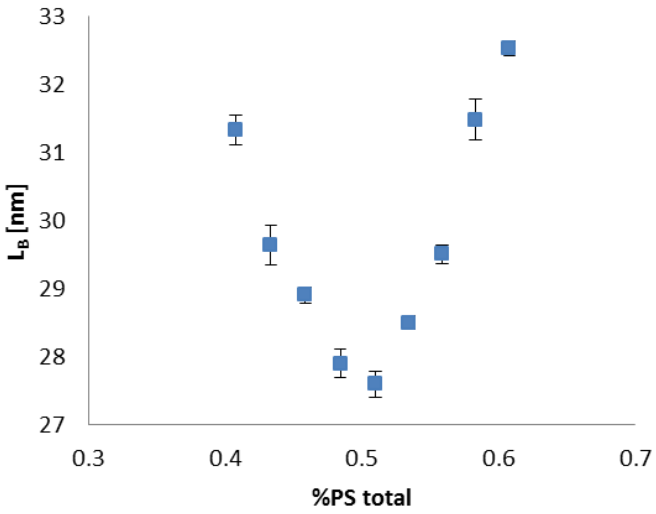

Figure 4-1. The domain spacing and overall volume fraction of PS change for BCP + HP binary blends. Error bars represent the standard deviation of the measurements.

The process flow that is illustrated in Figure 4-2 was used to fabricate chemical patterns and direct the BCP formulations. An 8 nm film of cross-linkable polystyrene (X-PS) is coated and thermally cross-linked. Photoresist is patterned and then plasma etched to define guide stripes in the X-PS. Remaining resist is stripped and a random copolymer brush is grafted to the exposed substrate. Block copolymer formulation is cast and annealed, and then plasma etching removes one domain and subsequently transfers the pattern into the substrate.

In order to compare the DSA behavior of BCP formulations with different domain spacings, the dimensions of the chemical pattern (pitch and guide stripe width) need to be normalized. The pitch of the chemical pattern, L_S, is normalized by L_S/L_B. The guide stripe width, W, is best normalized to the imposed domain spacing, L_S/n, where n is the density multiplication factor, which is three in this work. Therefore, the normalized guide stripe width is nW/L_S, which minimizes the covariance between L_S and W that would otherwise be present without proper normalization. In this way, all L_S have the same optimal normalized W.

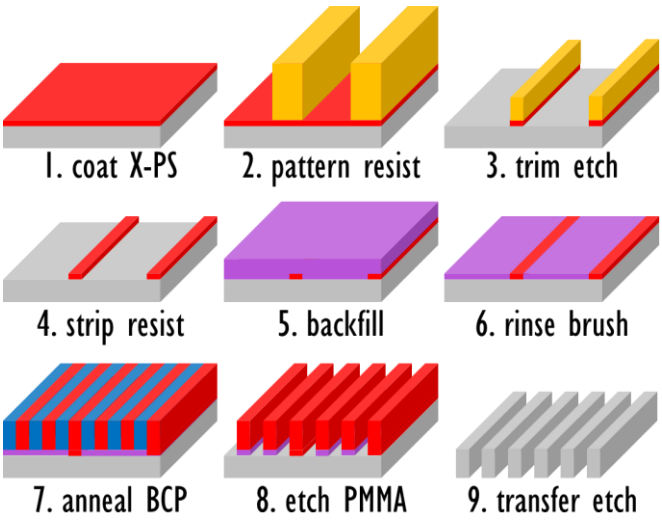

Figure 4-2. Schematic of processing steps used to fabricate chemical patterns and assemble BCP.

A. Commensurability analysis

The series of BCP formulations was assembled on chemical patterns with incremental pitches, guide stripe widths, and backfill brushes. A single SEM image with 2.75 x 2.75 μm field of view was used to assess the quality of assembly for each field. All fields are indicated in Figure 4-3 as either having misregistration defects or being defect-free. An axis-aligned ellipse is used to describe the range of defect-free conditions by minimizing the number of good and bad fields that are on the wrong side of the ellipse boundary. The dimensions of this ellipse quantify the threshold of geometric commensurability tolerance for the system to give well-aligned lamellae. Even though the defect density required to meet this threshold is high, it does set a limit such that comparisons among the processing parameters can be made.

Pitch commensurability tolerance and guide stripe width commensurability tolerance trend together. The PMMA-rich formulation has a consistent but narrow commensurability through backfill composition. The other two formulations have an abrupt change in commensurability tolerance when the %PS in the backfill is increased above the reference, consistent with previous work.[7]

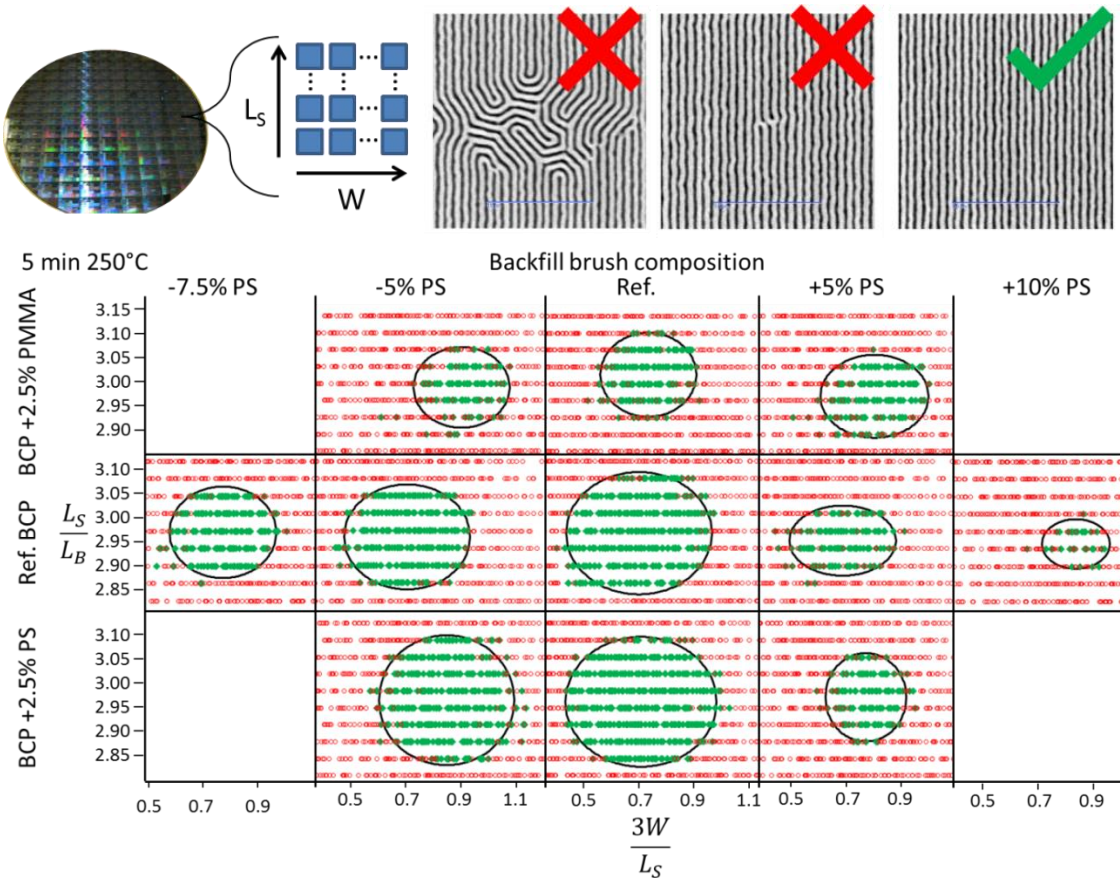

Range of $3W/L_S$ at best L_S/L_B

	Backfill composition %PS				
	-7.5%	-5%	ref.	+5%	+10%
BCP + 2.5%PMMA		0.177	0.299	0.320	
ref. BCP	0.386	0.455	0.524	0.312	0.120
BCP + 2.5% PS		0.463	0.563	0.245	

Range of L_S/L_B at best $3W/L_S$

	Backfill composition %PS				
	-7.5%	-5%	ref.	+5%	+10%
BCP + 2.5%PMMA		0.175	0.182	0.180	
ref. BCP	0.194	0.223	0.260	0.149	0.099
BCP + 2.5% PS		0.276	0.276	0.188	

Figure 4-3. BCP registration quality is plotted through a range of guide stripe dimensions with respect to BCP formulation asymmetry and backfill brush composition. All fields are distinguished as defect-free (green) or containing misregistration defects (red) in a representative SEM image. An axis-aligned ellipse marks the transition for each set of processing conditions and the range of the major and minor axis of each ellipse is color-coded from largest (green) to smallest (red).

Misregistration-style defects annihilate kinetically as long as the enthalpic gain exceeds the entropic penalty for the BCP to epitaxially align to the chemical pattern compared to alternative

domain arrangements.[8] The relationship between kinetic and thermodynamic limits of the commensurability analysis is explored in Figure 4-4, tracking three BCP formulations on the reference backfill at three annealing times. Additional annealing always increases the range of pitches and guide stripe widths that meet the assembly criterion, but the difference is significantly more dramatic from 1 minute to 5 minute anneal compared to the difference from 5 minute to 4 hour anneal, as the commensurability range approaches the maximum tolerance. Note that ultimate defectivity levels may continue to decrease in fields with pattern registration even after the commensurability range stops increasing.[9] The PMMA-rich BCP formulation consistently has lower commensurability tolerance than the other formulations for a given annealing condition, even after four hours of annealing at 250 °C.

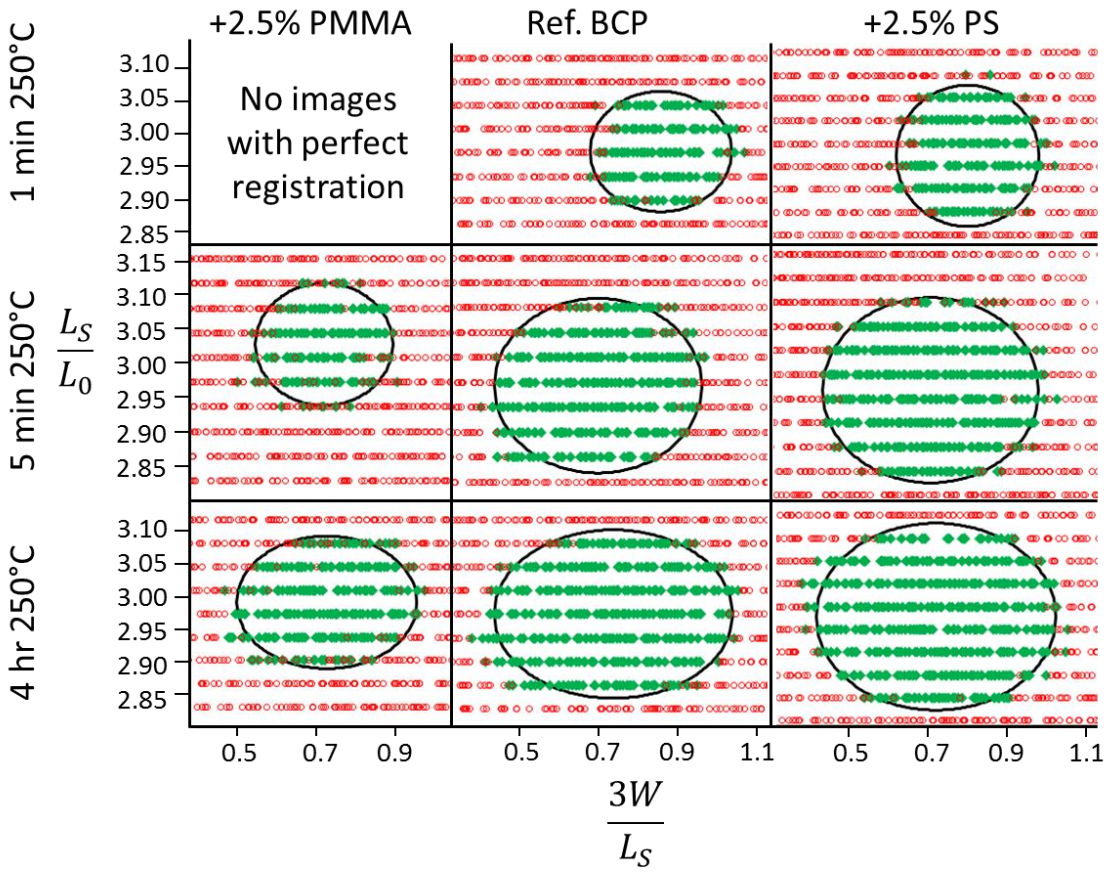

Range of $3W/L_S$ at best L_S/L_B

	BCP +2.5%PMMA	Ref. BCP	BCP +2.5% PS
1 min	0	0.342	0.359
5 min	0.299	0.524	0.563
4 hr	0.423	0.623	0.630

Range of L_S/L_B at best $3W/L_S$

	BCP +2.5%PMMA	Ref. BCP	BCP +2.5% PS
1 min	0	0.189	0.216
5 min	0.182	0.260	0.276
4 hr	0.206	0.266	0.295

Figure 4-4. Formulation kinetics process window for pattern registration defined by 1 SEM image per field. All formulations show an improved range of assembly between 1 minute and 5 minutes, but 4 hours of annealing does not lead to substantial improvement in commensurability tolerance range. An axis-aligned ellipse marks the transition for each set of processing conditions and the range of the major and minor axis of each ellipse is color-coded from largest (green) to smallest (red).

B. Defect modes

In addition to the commensurability analysis, optical defect detection and SEM review was performed on the 60 x 60 μm fields with an incremental pitch step size of 0.25 nm at optimum guide stripe width. Based on the SEM measurement of the guide stripe width, the center of the commensurability analysis is at $3W/L_s = 0.7$. This analysis focuses on misregistration defects, as the wafers were hand-coated and other defect modes are mitigated through filtration and automatic dispense.

Multiple misregistration categories were tracked, listed in Figure 4-5 with example images. A block copolymer dislocation consists of a branch point and end point. Two dislocations with opposing Bergers vectors localize the misalignment such that there is no misregistration beyond the pair. The arrangement of the dislocations in the style of a "V" dislocation pair results in misregistered jogs to not directly link the dislocations and is only observed when the BCP is compressed by the chemical pattern. Likewise, multiple pairs of dislocations can be found in a cluster, defined as having an overall Bergers vector of 0. Disclinations are defined by at least one domain looping back 180° without branching. Disclinations are nearly always associated with a larger misregistration cluster including dislocations. Separate classifications were made to distinguish when multiple defect clusters were found in the same review image.

For pattern conditions that support higher pitch commensurability, namely the reference BCP on reference backfill and PS-rich BCP on reference backfill, dislocation-style defects become dense even though disclinations are still rare. For the systems with narrower pitch commensurability in Figure 6, disclination-style defects are the majority defect mode at the limit of commensurability. From this observation, we attribute the reduction in commensurability to

weaker pattern registration and the stabilization of disclination-style defects. The trends in defects through pitch are representative of any direction through the commensurability ellipse except for V dislocation pairs, which were only observed under compression.

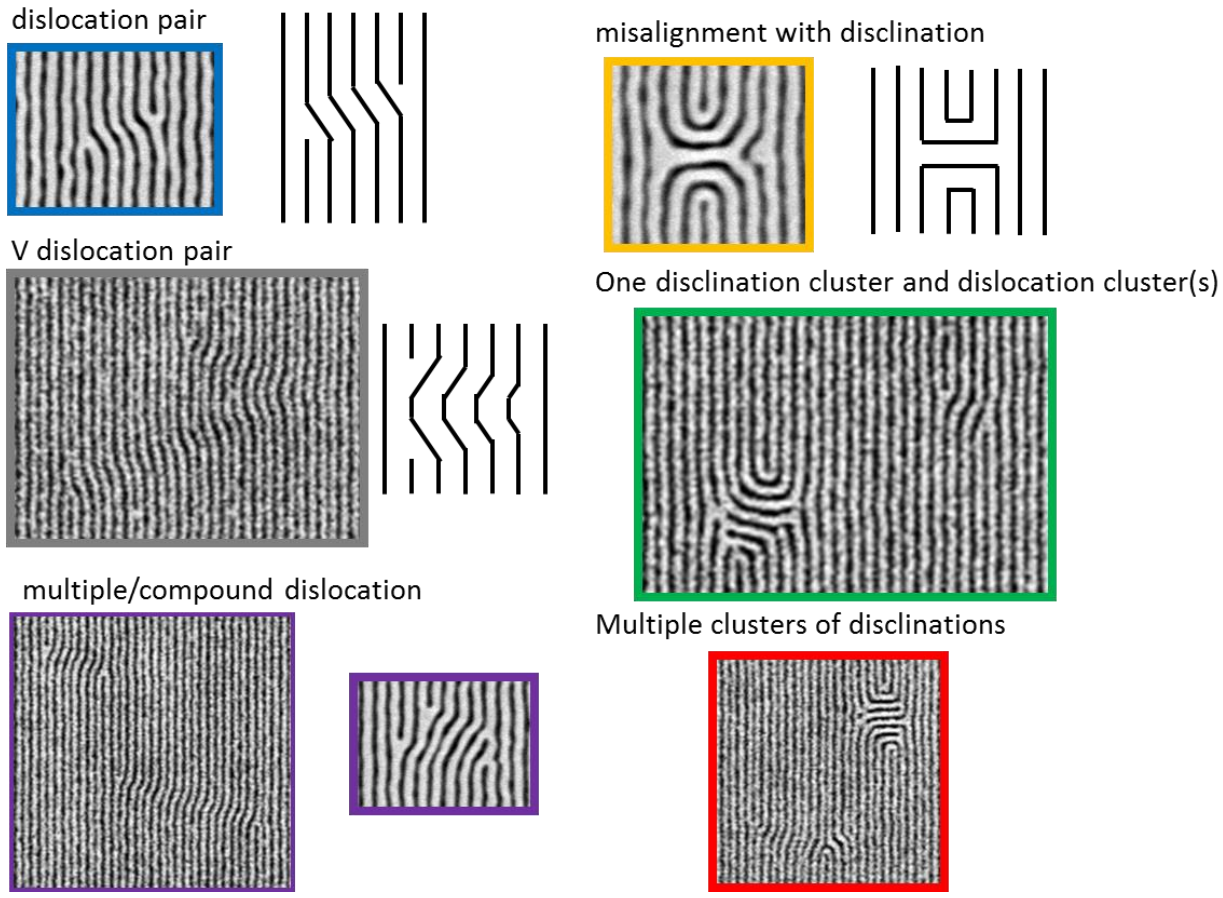

Figure 4-5. DSA misregistration-style defect categories are represented schematically and with example images. The left column only involves configurations of dislocation pairs whereas the right column always includes at least one disclination.

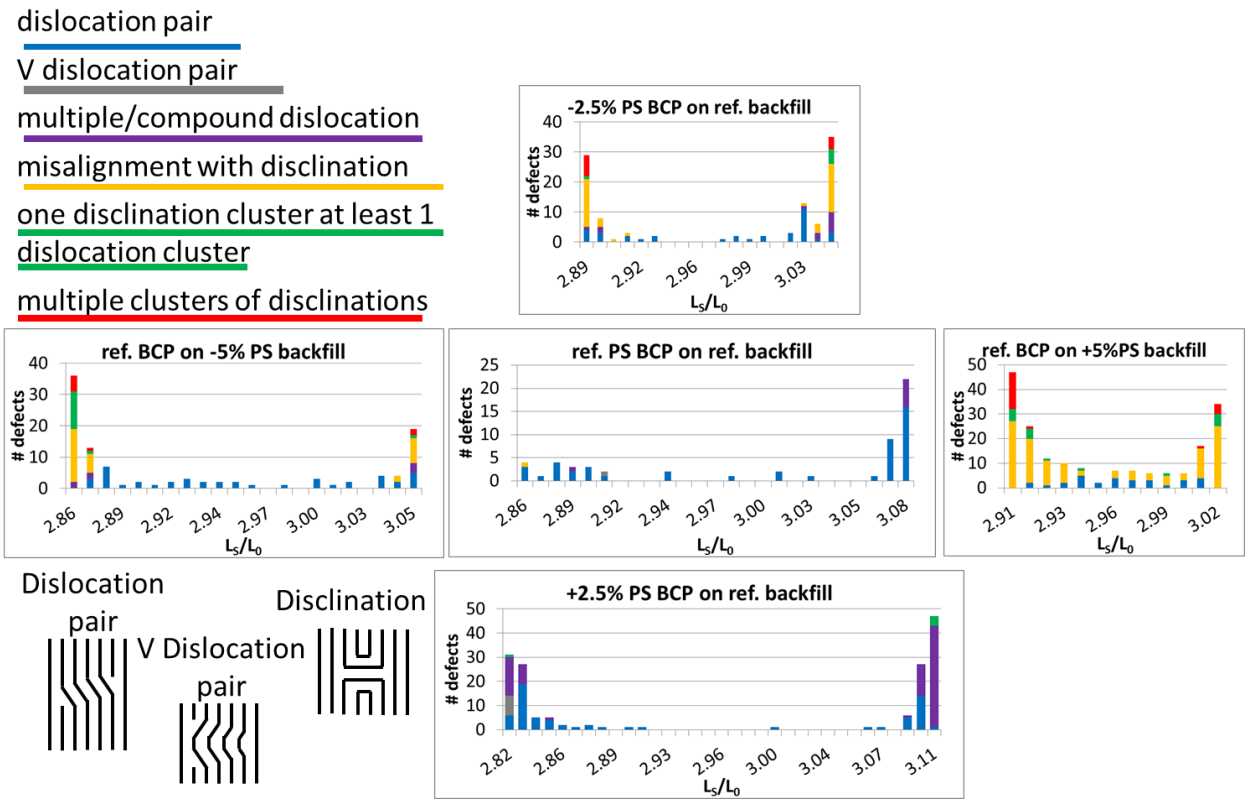

Figure 4-6. Defect review and classification identified misregistration defect modes through pitch at best guide stripe width. The conditions resulting in large commensurability tolerance are bounded by the dislocation-style defect whereas conditions resulting in narrower commensurability tolerance have predominantly disclination-style defects at the limit of assembly.

C. Microbridge formation

After transferring the DSA pattern into the Si, microbridges are present that were not visible in top-down SEM after PMMA removal. These features are likely due to a 3D structure in the original assembly. A representative SEM image was taken after Si etch for each misregistration-free condition in the commensurability analysis. The microbridges in each image were counted and plotted in Figure 4-7. A small background of microbridges may be attributable to hand-dispense conditions, but this does not account for the trends observed. More microbridges are found with increased PS composition in the BCP, increased PMMA composition in the backfill,

wider guide stripes, and narrower pitches. These features are not visible after PMMA is dry-etched, indicating that they are not through-film structures. Perhaps these microbridges indicate a transition to a perforated lamellae phase, however previous work[3] did not observe non-lamellar ordered morphologies with less than 10% BCP asymmetry. PMMA microbridges embedded in the PS domain would not be expected to be identified in this analysis as long as sufficient PS remained to mask pattern transfer, so it is unclear if this effect is symmetric with composition.

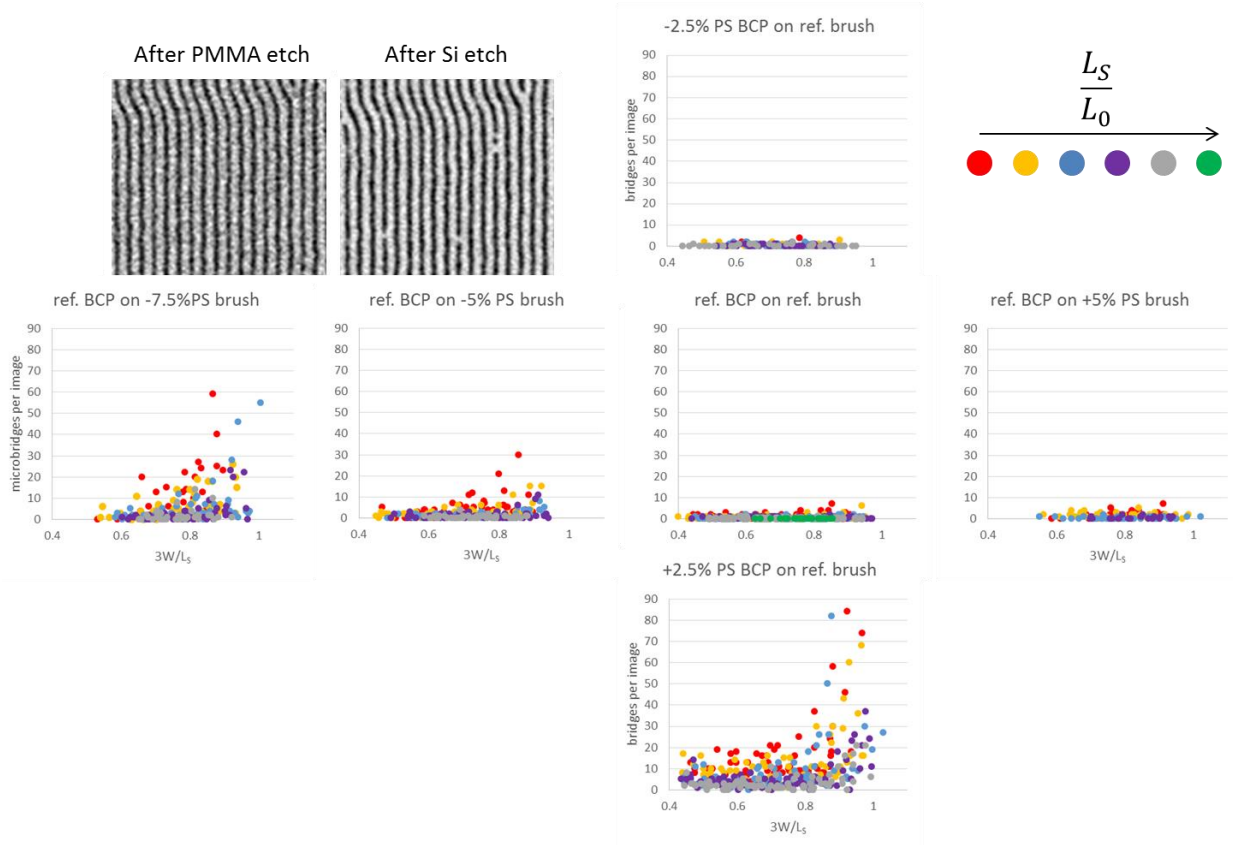

Figure 4-7. Microbridges were present after pattern transfer to Si, which were not observed after PMMA removal. The density of microbridges is a function of backfill composition, BCP composition, guide stripe width and pitch.

D. Comparison of BCP-HP to pure asymmetric BCP

The applicability of the work presented here is contingent on the premise that a BCP-HP blend has predictive performance to an asymmetric BCP. This premise can be rationalized by considering that the homopolymers used in this study have similar M_n to the corresponding block, so the system is in the dry brush regime.[ref] Therefore, the HP swells the domain by preferentially segregating to the center.

One PMMA-rich asymmetric lamellae-forming BCP was available, with a period of 28.5 nm and 45% overall PS content. After 5 min of annealing, neither the asymmetric BCP nor the corresponding BCP-HP blend resulted in a defect-free field of view, although partial registration was observed for a minimal range of CD/pitch. These observations are in agreement with the corresponding BCP + HP blend of equal volume fraction and is a natural extension of the behavior for the PMMA-rich BCP-HP blend considered above, that increasing PMMA volume fraction decreases pattern commensurability.

4-5 Conclusion

This work demonstrates how BCP formulation asymmetry influences DSA patterning performance in the LiNe flow. PMMA-rich formulations have narrower commensurability tolerance in both pitch and guide stripe width compared to that of the reference or PS-rich formulations. Disclination-containing defect clusters define the commensurability limit when pattern registration is weak, but dislocation pairs without disclinations are observed when the commensurability tolerance is broad. This difference in commensurability tolerance is associated with a different defect mode that dominates at the commensurability limit. Systems that have smaller commensurability tolerance have disclination-style defects dominate at the

commensurability limit whereas systems with larger commensurability tolerance have dislocation pairs at the commensurability limit, even to high density before observing disclinations. Therefore, the presence of disclinations is an indication that the system has poor pattern registration. Despite PS-rich formulations having a large commensurability tolerance, non-through-film microbridge structures formed in high density and interfered with pattern transfer. Control over the BCP formulation is critical to achieve the low defect densities needed for microelectronics applications of DSA.

4-6 References

1. Nagpal, U.; Mueller, M.; Nealey, P. F.; de Pablo, J. J. *Acs Macro Letters* **2012,** 1, (3), 418-422.

2. Li, W.; Nealey, P. F.; de Pablo, J. J.; Mueller, M. *Physical Review Letters* **2014,** 113, (16), 8301-8301.

3. Khandpur, A. K.; Forster, S.; Bates, F. S.; Hamley, I. W.; Ryan, A. J.; Bras, W.; Almdal, K.; Mortensen, K. *Macromolecules* **1995,** 28, (26), 8796-8806.

4. Campbell, I. P.; Lau, G. J.; Feaver, J. L.; Stoykovich, M. P. *Macromolecules* **2012,** 45, (3), 1587-1594.

5. Liu, C.-C.; Thode, C. J.; Delgadillo, P. A. R.; Craig, G. S. W.; Nealey, P. F.; Gronheid, R. *Journal of Vacuum Science & Technology B* **2011,** 29, (6).

6. Jeong, U.; Ryu, D. Y.; Kho, D. H.; Lee, D. H.; Kim, J. K.; Russell, T. P. *Macromolecules* **2003,** 36, (10), 3626-3634.

7. Delgadillo, P. A. R.; Gronheid, R.; Lin, G.; Cao, Y.; Romo, A.; Somervell, M.; Nafus, K.; Nealey, P. F. *Proc. SPIE Advanced Lithography* **2013,** 8680, 86801H-1.

8. Nealey, P. F.; Edwards, E. W.; Stoykovich, M. P.; Mueller, M.; de Pablo, L. J. *Abstracts of Papers of the American Chemical Society* **2005,** 230, U4121-U4121.

9. Delgadillo, P. A. R.; Harukawa, R.; Parnell, D.; Lee, Y.-T.; Chan, B. T.; Lin, G.; Cao, Y.; Nagaswami, V. R.; Somervell, M. H.; Nafus, K.; Gronheid, R.; Nealey, P. F. *SPIE Advanced Lithography* **2014,** 9049, 9049-19.

Chapter 5:

Macrophase Separation of Blends of Diblock Copolymers in Thin Films

5-1 Abstract

Symmetric poly(styrene-*b*-methyl methacrylate) block copolymers (BCP) with total molecular weights of 129-412 kg/mol were blended with a symmetric 44 kg/mol BCP. This set of polymers covers the parameter space of molecular weight ratios of the large vs small BCP in the pair, $R = M_{n,L}/M_{n,S}$ from 2.9 to 9.4. The blends macrophase separate into a nearly pure small period phase and a blended large period phase when R is greater than five. The influence of film confinement on the phase behavior of these blends was analyzed by comparing the morphology within films on nonpreferential substrates and bulk samples using scanning electron microscopy and x-ray scattering techniques. In the thin film, the large period phase has approximately equal volume fraction of the high and low molecular weight BCP, but in the bulk, the large period phase is more concentrated with the high molecular weight BCP. This difference in the saturation composition not only narrows the composition window for macrophase separation but also results in a 12% decrease of the large saturated period in the thin film compared to the bulk behavior of the same polymer blend. The period of the small period phase in all macrophase separating blends is comparable to that of the pure short BCP. When both phases are present, the quantity of each phase is described by the lever rule. Furthermore, when the molecular weight ratio is near the critical molecular weight ratio for macrophase separation, the blends have a transition behavior that has similarities to both the miscible and macrophase separating systems.

5-2 Introduction

The self-assembling nature of block copolymer (BCP) films has garnered a great deal of scientific interest due to potential application in a variety of fields that have use for patterned nanoscale features.[1-3] BCPs can be blended with homopolymer[4-9] as well as with other BCPs[10-13] to tailor properties such as the domain spacing, mobility and morphology of the uniform microdomain structure. However, BCP-BCP blends are not limited to being miscible, even when they have the same chemistry.[14-22] Instead of forming a single periodic structure, blends with substantial difference in molecular weight macrophase separate into two microdomain structures in equilibrium with each other. Through the assembly of different sized microstructures in the same film, new possibilities for template applications may be realized.

Two parameters govern the phase behavior of a blend of symmetric BCPs. One parameter is the ratio of the molecular weight of the large BCP to the small BCP, $R = M_{n,L}/M_{n,S}$; the other parameter is the concentration of the large BCP in the polymer melt given as the volume fraction, φ_L. Previous studies have demonstrated that a blend of symmetric BCPs macrophase separate when $R > 5$ and $\varphi_L < 0.6\text{-}0.7$ for bulk systems. Blends of symmetric poly(styrene-*b*-isoprene)[19,21] and poly(styrene-*b*-butadiene)[17] have an experimental phase diagram for macrophase separation in quantitative agreement with Matsen's self-consistent field theory (SCFT) phase diagram.[18]

While the phase behavior of macrophase separation of BCP-BCP blends has been explored in bulk systems, comparatively little is known about them in thin films. Papadakis et al demonstrate that spin-coating a BCP-BCP blend capable of macrophase separation leads to a single, blended period, and additional mobility is needed to achieve macrophase separation.[23] Regarding thermodynamic confinement effects, a higher composition of homopolymer has been shown to

mix miscibly with a BCP as a thin film compared to the bulk, suggesting that confinement influences the macrophase separation behavior of polymers.[24] The goal of this study is to characterize the impact of interfaces and confinement on the assembly of block copolymer blends that macrophase separate into two microstructures due to the difference in molecular weight.

5-3 Experimental Section

A. Materials

Poly(styrene-*b*-methyl methacrylate) (PS-*b*-PMMA) BCPs listed in Table 5-1 were purchased from Polymer Source, Inc., and used as received. P($S_{57\%}$-*r*-$MMA_{39\%}$-*r*-$GMA_{4\%}$) random copolymer was synthesized as described previously.[25] Prime silicon < 100> wafers were purchased from WRS Materials and cleaned with piranha solution (3:7 v/v 30% H_2O_2:H_2SO_4) at 130 °C for 30 min, rinsed with deionized water and dried under N_2 flow before use. Toluene (certified ACS grade) was purchased from Fischer Scientific and was used without further purification.

Table 5-1. Characteristics of PS-*b*-PMMA

Designation	M_n(PS) - M_n(PMMA) (kg/mol)	PDI
SM44	22-22	1.09
SM129	66-63	1.08
SM211	105-106	1.13
SM320	160-160	1.09
SM412	205-207	1.16

B. Film Preparation and Characterization

A 0.2 wt % solution of cross-linkable random copolymer in toluene was spin-coated onto clean silicon wafer at 4000 rpm and cross-linked under atmospheric nitrogen at 250 °C for 5 min.

Separate solutions of 2 wt % polymer in toluene were prepared for each BCP. SM44 was blended with each other polymer from Table 1 in 10 wt % increments. These blended solutions were spin-coated at 4000 rpm onto the modified silicon to give a 60 nm thick film. While the thickness of a thin film is often scaled to the domain spacing (L_0) of the target polymer, some films in this study have multiple domain spacings. Therefore, a single film thickness was used for all blend compositions. A few select blend compositions were also prepared at higher concentration and cast 400-800 nm thick. The polymer films were then annealed at 250 °C for 24 h under vacuum conditions in order to minimize the degradation of polymer.

The film thickness of each sample was measured with a Rudolf Research/Auto EL II nulling ellipsometer using three wavelengths (405, 632, and 830 nm) with an incidence angle of 70° to the sample. FilmEllipse software (version 1.1, Scientific Co., Intl.) was used to calculate the film thickness from the ellipsometry measurements. Scanning electron microscopy (SEM) imaging was performed with a LEO 1550VP field emission scanning electron microscope operating at 1 kV accelerating voltage. The characteristic periods in the thin films were determined from plan-view SEM images with two techniques: 1. Fast Fourier Transform (FFT) analysis and 2. Measurements across multiple periods where the polymer has low curvature was averaged. The area fraction of each phase was determined using AxioVision LE image analysis software by Zeiss. The phase boundary was defined with the outline tool and the area enclosed by the outline was calculated by the software. The area fraction of the large period phase, a_L, is defined as the area of the large period phase divided by the total analysis area. Grazing incidence small angle x-ray scattering (GISAXS) was performed at Argonne National Laboratory's Advanced Photon Source beamline 8-ID-E with a 7.35 keV beam. Incidence angle α = 0.16°-0.24° were used to

probe different penetration depths of the films. A Pilatus CCD detector was placed 2.17 m from the sample to collect the 2D spectra and data processing was carried out using Matlab software developed on the beamline.

C. Bulk Sample Preparation and Characterization

Bulk polymer samples of polymer blends were prepared by blending 5 wt % solutions of polymer in toluene, then evaporating the solutions in standard aluminum DSC pans. Additional solution was added until the dry samples were about 1 mm thick. Next, they were annealed at 250 °C for 24 h under vacuum, using a 1 °C/min ramp increase to prevent foaming due to retained solvent.

The period of the bulk polymer samples was measured with a Rigaku Cu K_α small-angle X-ray scattering (SAXS) instrument (8.04 keV) with the detector placed 2 m from the sample. The working voltage was 45 kV and the current was 0.9 mA. The SAXS experiments were carried out at room temperature.

5-4 Results and Discussion

Four high molecular weight symmetric BCPs were blended with a single low molecular weight symmetric BCP at different blend compositions. Thin films of these blends were analyzed with respect to the molecular weight ratio of the polymers in the blend and the blend composition. Silicon wafer substrates were initially modified by cross-linking a random copolymer of PS and PMMA containing 57% PS, which is suitable to form perpendicularly oriented lamellar structures in thin films of symmetric PS-*b*-PMMA.[25] Next, a BCP film was spin-coated 60 nm thick and annealed at 250 °C for 24 h under vacuum conditions. These films were analyzed by SEM, enabling the measurement of both the period and area fraction of each phase.

Representative plane-view SEM micrographs of films containing each polymer pair for a series of blend compositions are shown in Figure 5-1. The volume fraction of the large BCP, φ_L, increases from left to right; the molecular weight of the large polymer increases from bottom to top. As the molecular weight of the large polymer increases, the ratio of the molecular weights of the large vs small polymer in the pair, R, also increases. Across this parameter space, films are either miscible and have a single domain spacing, or macrophase separated and form regions of large and small domain spacings. Macrophase separation behavior is only observed in the blend composition series SM320/SM44 and SM412/SM44 (R = 7.3 and 9.4), in the range $0.1 \leq \varphi_L \leq 0.4$ (highlighted in red). The blend composition series SM211/SM44 and SM129/SM44 (R = 4.8 and 2.9) do not exhibit an identifiable macrophase separation. However, blend composition series SM211/SM44 in the range $0.1 \leq \varphi_L \leq 0.3$ (highlighted in blue) has junctions that exhibit swelling such as the circled structures, differentiating these images visually from the typical fingerprint morphology. Also note that pure SM412 has slow dynamics, so it does not have well-formed lamellae despite the intense annealing conditions.

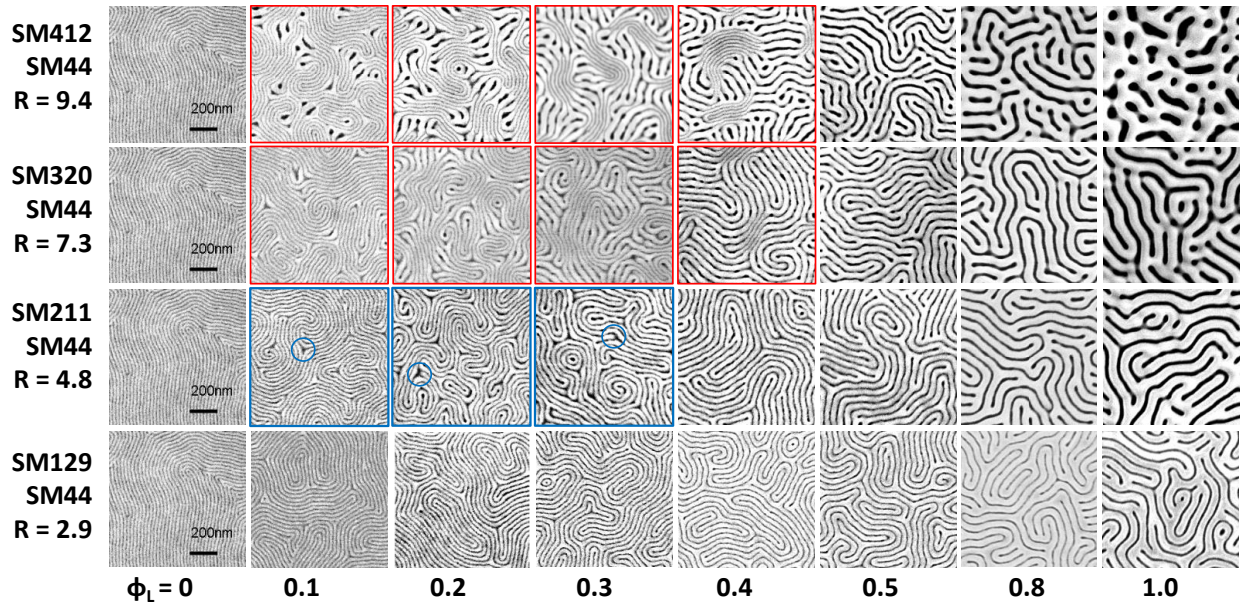

Figure 5-1. Representative SEM images of each blend series at different volume fractions spanning the composition range of macrophase separation. The red highlighted images have macrophase separation. The blue highlighted images show transition behavior. The circles indicate swelled junctions in a transition behavior from miscible blend series to macrophase separating series.

The periodicities of each phase formed in each film were measured from the SEM images. Two techniques were used in order to collect these data. Fast Fourier Transform (FFT) image analysis generated intensity vs. wave vector profiles, with primary peaks in intensity corresponding to the period of the polymer. Real-space measurement of the average period within the SEM images both confirmed the FFT results and provided measurements of the small period phase for φ_L= 0.4, when the corresponding primary peak in the FFT analysis was not identifiable above the background. An example of these two techniques is illustrated in Figure 5-2.

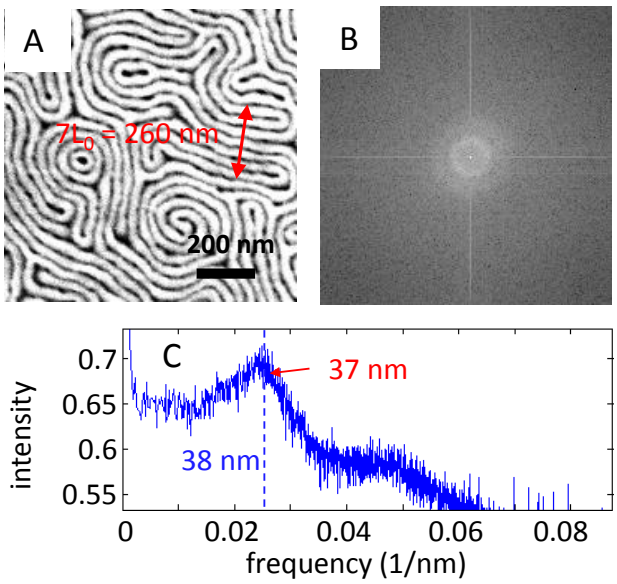

Figure 5-2. The domain spacing for SM211/SM44 φ_L = 0.3 was measured by two techniques: 1. Using FFT by calculating the FFT power spectrum (B) from the SEM image (A), then averaging the power spectrum (C) and identifying the primary peak(s). 2. Real-space measurement was achieved by identifying low-curvature segments and measuring the distance across multiple periods (A). Both techniques were repeated to average the domain spacing.

Every film from the blend composition series SM211/SM44 and SM129/SM44 had a single characteristic period, as observed in Figure 5-3A. Matsen originally derived the period scaling for miscible blends of symmetric block copolymers using the strong segregation regime (SSR) assumption.[18] This theory was modified to fit the experimental measurements of PS-*b*-PMMA films using a fit parameter, ν, in equation 1, where x_L is the molar fraction of the long polymer and $L_{0,L}$ is the period of the neat assembly of the long polymer.[13] For a blend of two polymers in the SSR limit, ν = 2. Experimentally, ν ranges from 1.7 to 5.7 to account for intermediate and weak segregation regime behavior.[13] The thin film domain spacing data in Figure 5-2A are described well with this equation using ν = 3.2 for SM129/SM44 and ν = 1.5 for SM211/SM44.

$$L_{0,blend} = L_{0,L} \frac{\left[\frac{1}{R}+x_L\left(1-\frac{1}{R}\right)\right]}{\left[\frac{1}{R}+{x_L}^{\nu+1}\left(1-\frac{1}{R}\right)\right]^{1/\nu+1}} \qquad (5\text{-}1)$$

The period analysis for the macrophase separating blend composition series, SM320/SM44 and SM412/SM44, are given in Figure 3B. The modified SSR equation can capture the single-phase behavior, where $\varphi_L \geq 0.5$ using $\nu = 1.5$. In the two-phase regime, two periods are observed and the period of each phase is independent of composition. This observation indicates that the two phases have constant compositions, as expected from thermodynamic two-phase equilibria. Furthermore, the small period phase has the same period as the neat assembly of the small block copolymer, which is in agreement with previous studies on bulk samples of macrophase-separating blends.[15, 21]

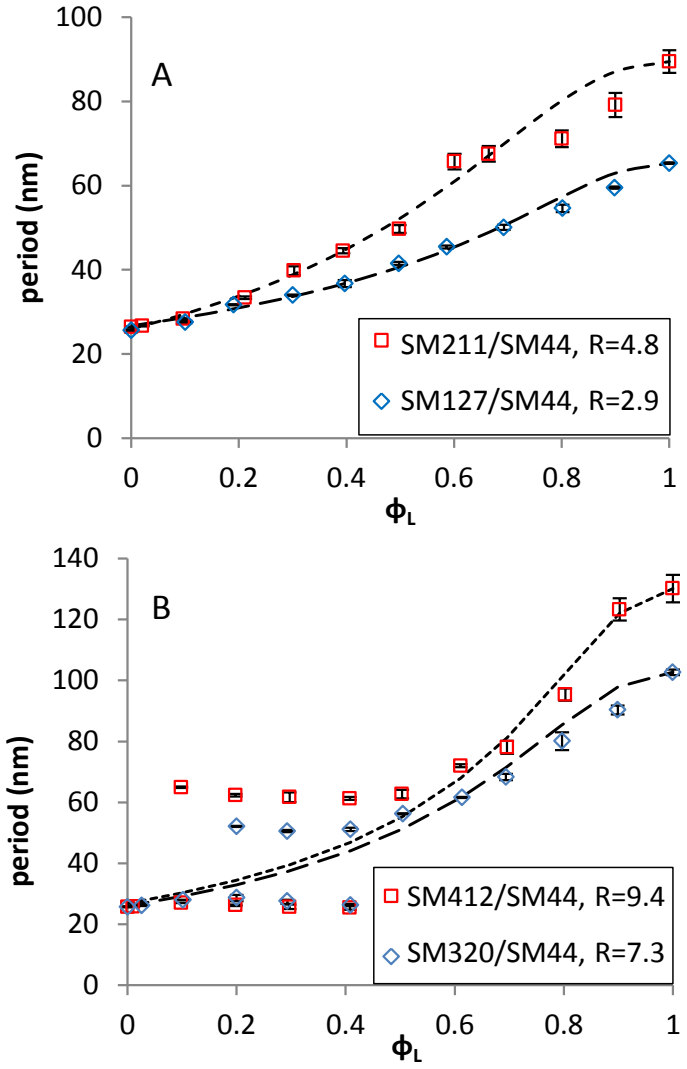

Figure 5-3. Period analysis and modeling of blends with respect to composition for (A) miscible blend series SM129/SM44 and SM211/SM44, and (B) macrophase separating series SM320/SM44 and SM412/SM44. Error bars indicate one standard deviation of error.

If the macrophase separation behavior follows standard thermodynamic binary phase equilibria, the quantity of each phase is expected to be governed by the lever rule. Note that the assumption of thermodynamic phase equilibria is valid as long as the composition of the respective phases is not kinetically limited; once phase separation is achieved, additional mobility is expected to result in grain coarsening. Furthermore, if the film thickness is uniform

and the phase behavior does not form a gradient through the thickness of a film, then the area fraction of a phase in an SEM micrograph is the same as its volume fraction. The large and small period phases are not expected to overlap, as the films are on surfaces that induce perpendicular alignment of lamellae. The area fraction of the large period phase was measured using AxioVision LE image analysis software by Zeiss. Results for the samples that displayed macrophase separation (highlighted in red in Figure 1) are shown in Figure 5-4. Area fraction measurements were independent of SEM image magnification and consistent from image to image of the same sample, so the reported area fraction is representative of the sample. The area fraction is linear with respect to φ_L, as expected for two-phase equilibria, where the composition of each phase is fixed, but the amount of each phase adjusts to account for the overall composition. Based on this relationship, the composition at the phase boundary can be extracted from extrapolating the area fraction to a value of 0 and 1. Using this approach, 2-phase behavior is expected in the range of $0.05 < \varphi_L < 0.45$ for SM320/SM44 and $0.003 < \varphi_L < 0.49$ for SM411/SM44. These values are in agreement with the observation that no macrophase separation is seen in the SEM images at $\varphi_L = 0.5$. The purity of the short block copolymer in the small period phase confirms the analysis of the earlier observation that the period of the small period phase closely matches the neat small block copolymer period. These observations can be understood by picturing the small period polymer saturating the A-B interface of the large period phase and excess small period polymer becoming excluded into a separate phase.

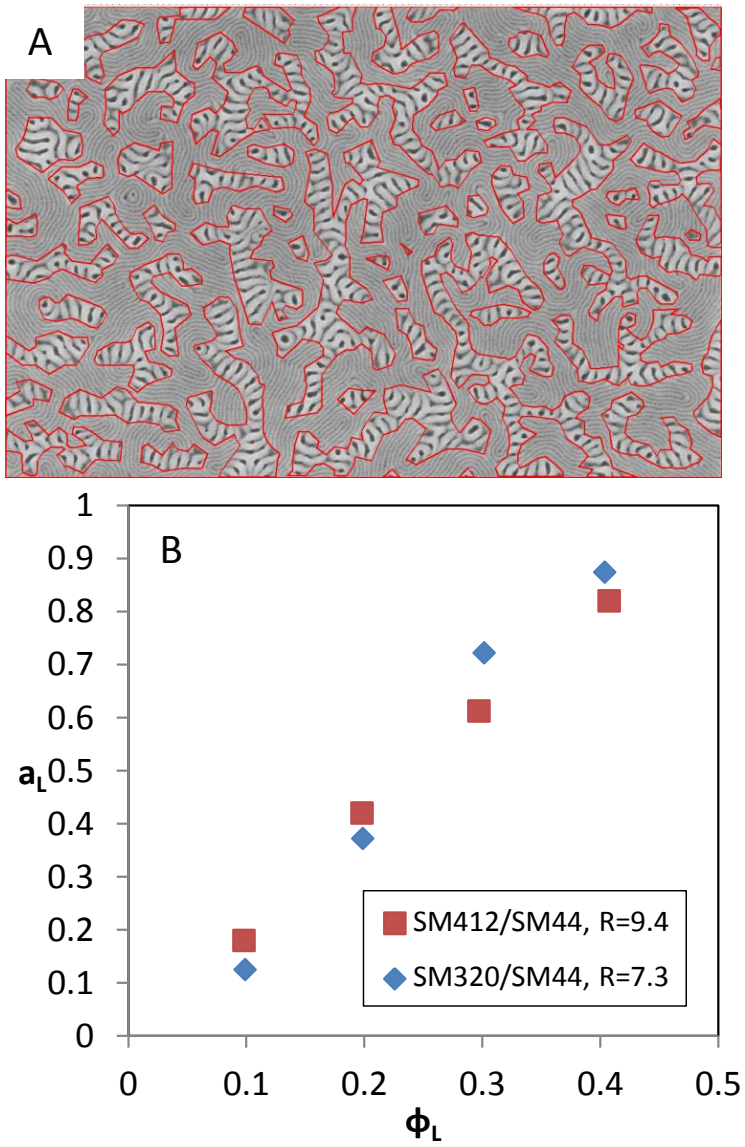

Figure 5-4. The area fraction of the large period phase (a_L) is measured by manually defining the phase boundary in Axiovision software (A). The area fraction of the large period phase is given with respect to the blend fraction for SM412/SM44(squares) and SM320/SM44(diamonds) (B). A linear relationship is expected for standard thermodynamic two-phase equilibria. The small period phase is nearly pure of the short block copolymer and the large period phase is less than $\varphi_L = 0.5$ for both blend series.

The critical composition of macrophase separation measured in the thin film, $\varphi_L < 0.5$, is slightly lower than what has been observed in bulk both experimentally[15, 17] and in simulations[18]. In order to isolate the effect of film confinement as opposed to other factors such as the specific

polymer chemistries, we now examine the bulk behavior of the macrophase separating blend systems. The bulk samples were prepared by evaporating the polymer from toluene and annealing them at 250 °C for 24 h in vacuum conditions. The SAXS profiles for three series of blend compositions taken at room temperature are shown in Figure 5-5. The beamstop at q = 0.06 nm^{-1} blocks the primary peak for pure SM412 and SM320. However, assuming a lamellar morphology, the secondary peaks point to the position of the expected primary peak. Using this method, all profiles of pure samples correspond to an L_0 that is nearly identical to that of the thin film measurement. A summary of key domain spacings from bulk and thin film are presented in Table 5-2. All of the blended samples for SM412/SM44 and SM320/SM44 have two primary peaks. One lines up with the pure SM44 and the other lies between the pure polymers composing the blend. However, the large period phase in the bulk samples is about 12% larger than the equilibrium large period phase measured in the thin film.

Table 5-2. Comparison of the period of each phase for the film and bulk samples.

L_0 of film/bulk (nm)	SM211 SM44	SM320 SM44	SM412 SM44
Pure large	89/91	103/102	130/130
Large phase	*/46	52/59	63/72
Small phase	*/30	27/27	26/27

Since the volume fraction of the phases is not readily extracted from SAXS directly, a different approach is taken to estimate the phase behavior for the bulk. Equation 5-1 relates the blend composition to the miscible period, so the domain spacings of the macrophase-separated blends correspond to the compositions at the phase boundaries. By applying this approach to the bulk domain spacings, macrophase separation is expected for $0.01 < \varphi_L < 0.64$ for SM411/SM44, $0.02 < \varphi_L < 0.62$ for SM320/SM44, and $0.1 < \varphi_L < 0.42$ for SM211/SM44, which are plotted in Figure 5-6. These estimates for the range of φ_L for macrophase separation in the bulk are wider than the estimates for the thin film mentioned above. This difference is further evidenced by the presence of the SAXS peaks corresponding to the small period phase at $\varphi_L = 0.5$ for the bulk samples whereas no small period phase is observed in the thin film images at the same composition. This observed difference in phase equilibria behavior between thin film and bulk deserves additional work to probe the mechanism that accounts for the discrepancy.

The blend series SM211/SM44 also has two primary peaks at $\varphi_L = 0.25$, but neither corresponds with the pure SM44. These peaks could be related to the swelled junctions observed in the thin films from $\varphi_L = 0.1 – 0.3$, however these peaks are distinct, unlike the FFT or real-space measurements for the thin films, suggesting that distinct phases are present for the bulk sample. The $\varphi_L = 0.5$ sample has a single primary peak that matches the period of the corresponding thin film at 49 nm, however the higher order peaks are extremely weak and broad, indicating that the long-range order is very poor or non-lamellar structures are present.

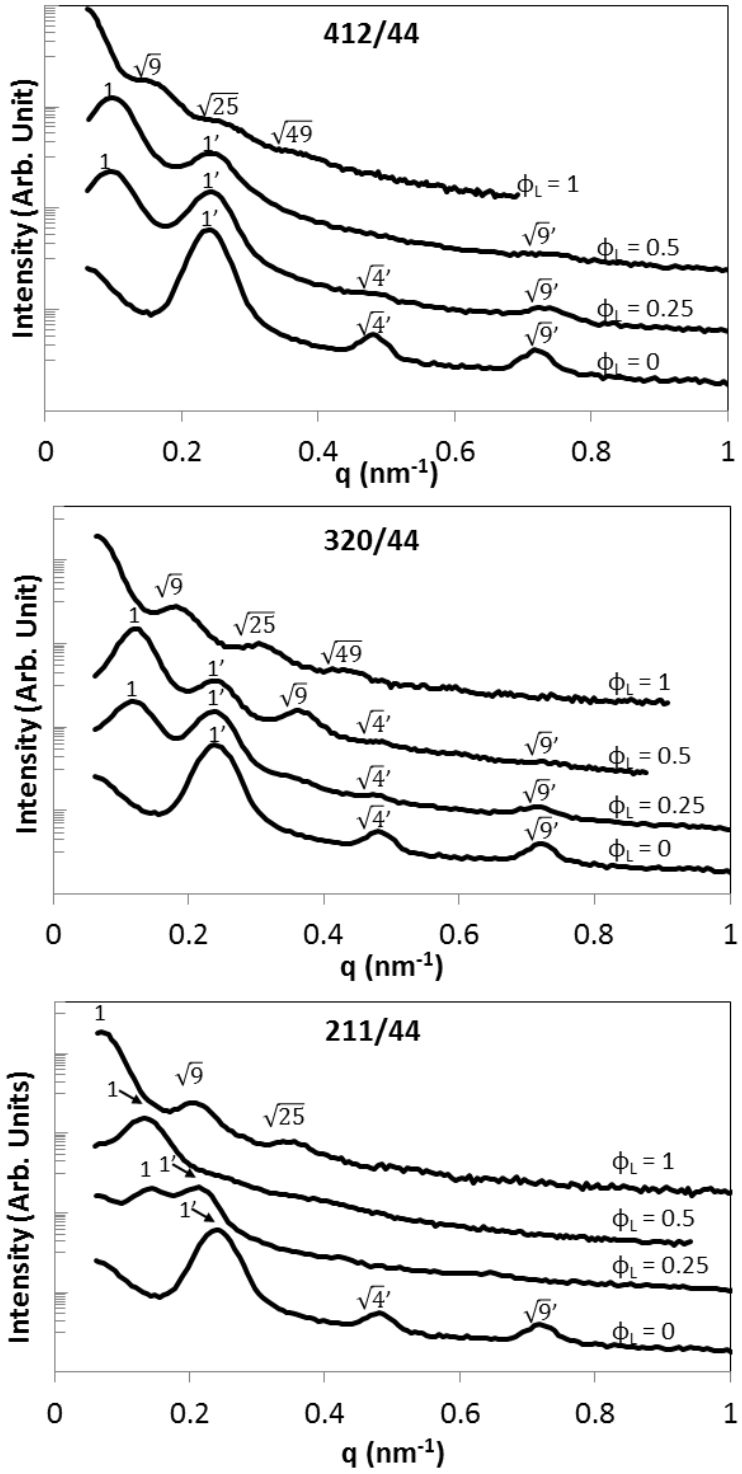

Figure 5-5. SAXS traces of bulk PS-b-PMMA blends at different blend fractions taken at room temperature after annealing. Peaks designated with a prime correspond to a separate small period phase.

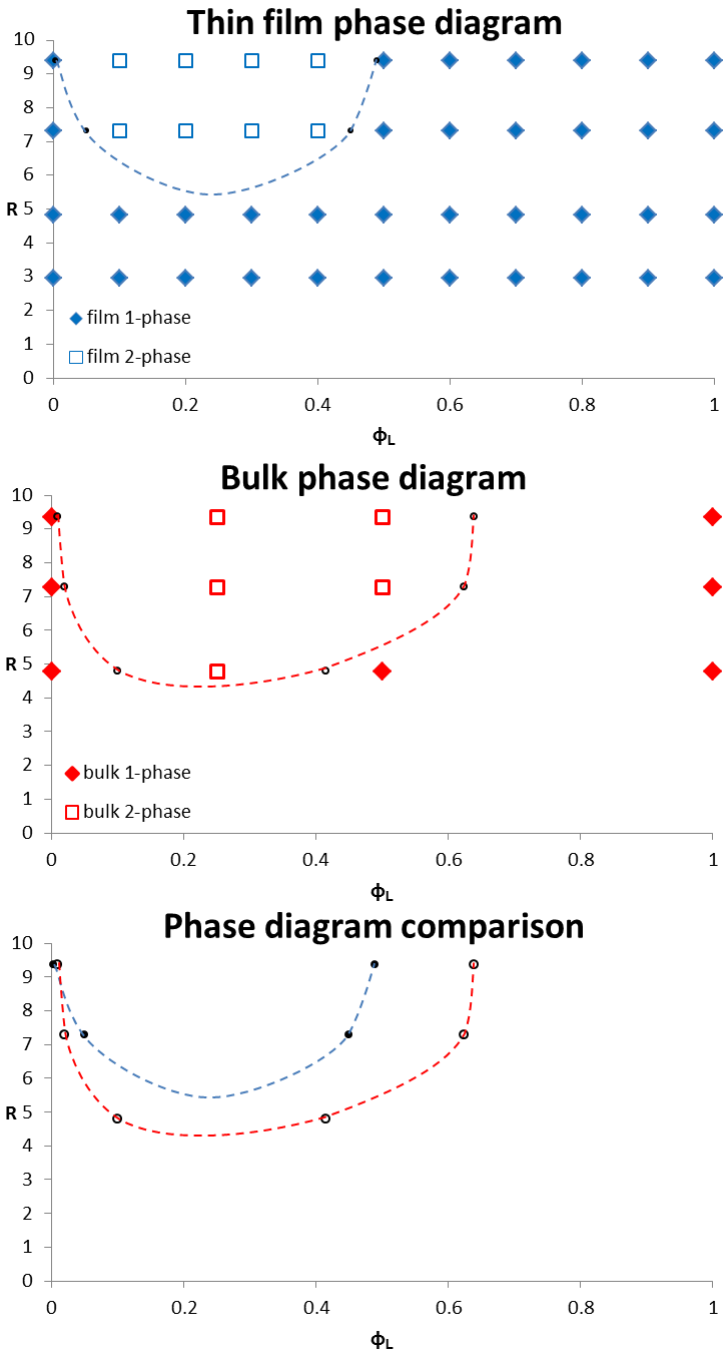

Figure 5-6. Phase diagram of the BCP-BCP macrophase separation for thin film and bulk. Thin film phase boundary points are from area fraction analysis in Figure 4 extrapolated to the phase boundary. Bulk phase boundary points are from comparing the period of the phase separated domains to the miscible period analysis in Figure 5-3. Lines guide the eye through the phase boundary points.

In light of the differences in phase behavior exhibited by the thin film and bulk, thick films were used to investigate the transition from thin film to bulk. The blend SM412/SM44 with composition $\varphi_L = 0.5$ was spincast into films 520 nm and 830 nm thick, which are larger than the domain spacing of the microstructures. These films were probed with grazing incidence small angle x-ray scattering (GISAXS) at incidence angles between $\alpha = 0.16°$ and 0.24°, which correspond to the critical angles of the polymer and substrate, respectively. Representative 2D GISAXS spectra are shown in Figure 7, where the film thickness increases from top to bottom and the angle of incidence increases from left to right. The spectra for the 60 nm film have a single primary peak corresponding to $L_0 = 63$ nm and the film morphology shows no variation with depth, as probed with different incident angles. On the other hand, the spectra of the films that are 520 nm and 830 nm thick have peaks corresponding to $L_0 = 63$ nm and 25 nm, indicating that the blend has macrophase separated. While the large period phase measurement is not significantly different than the thin film, the presence of the small period phase indicates a transition toward the behavior of the bulk polymer sample at this composition. As previous work has shown, the influence of a surface can extend to quite thick films.[26] Also, the relative intensity of the peak for the small period phase is strongest at an incidence angle of 0.16°, when the beam has the shallowest penetration depth. From this observation, we infer that the small period phase preferentially segregates to the free surface, which is in agreement with previous work.[23] The large period phase peaks form arcs, which are attributed to a distribution of the orientation of the large period phase with respect to the surface normal.

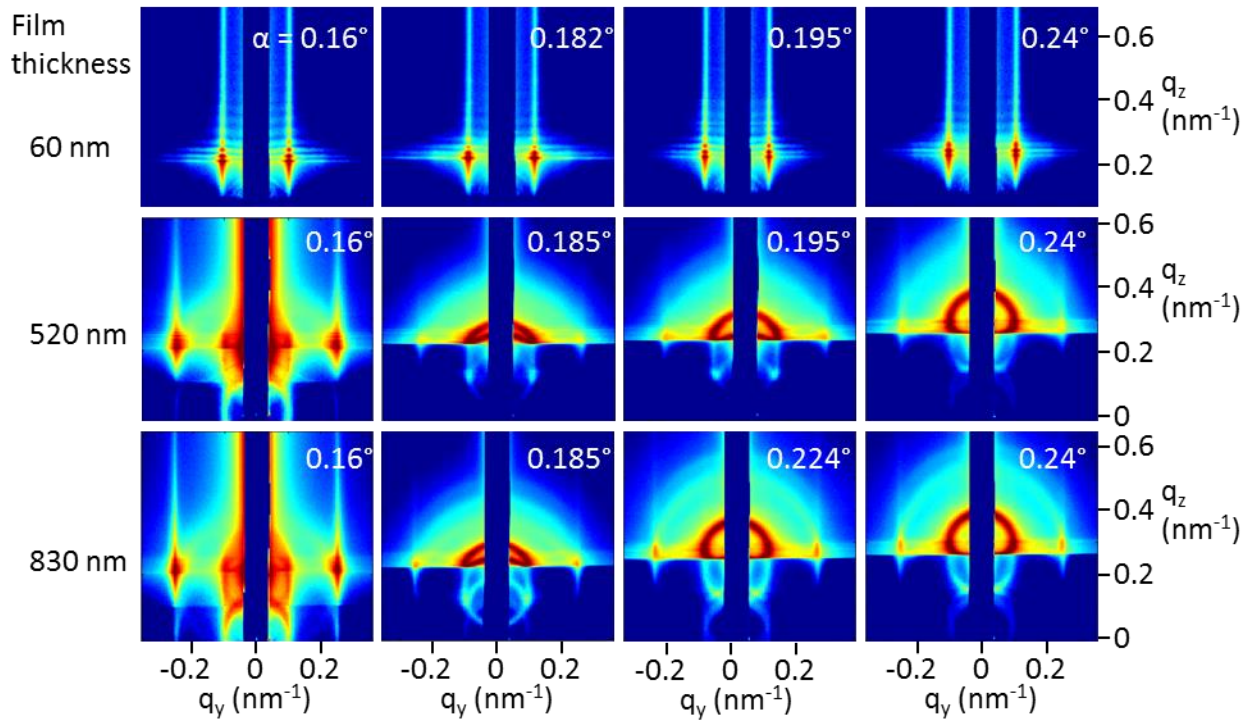

Figure 5-7. GISAXS spectra of SM412/SM44 $\varphi_L = 0.5$ at different film thicknesses and incident angles. While the 60 nm film has no indication of small period phase, the thicker films have a coexistence of both phases.

5-5 Conclusion

This work characterizes the macrophase separation of symmetric block copolymers in thin films and draws comparisons to the bulk behavior. The critical molecular weight ratio for macrophase separation is around five, which is in agreement with other polymer systems.[18, 19] The equilibrium composition was determined by equating the area of a thin film to its volume. From this analysis, the small period phase is nearly pure of the small BCP and the large period phase has a volume fraction of less than 50% of the large BCP. The measurement of the period as a function of composition is in agreement, where the period of the large period phase is constant below this critical composition. When the film thickness is increased, a blend of $\varphi_L = 0.5$ switches from miscible to macrophase separating and the small period phase

preferentially segregates to the free surface. In the bulk, the large period phase is larger than that of the films, pointing to a higher critical composition of macrophase separation, which compares to other polymer systems.[15, 17, 18] It is still uncertain whether the true equilibrium is affected by film confinement or if these observations result from assembly kinetics or some other mechanism. With the current focus of thin films of block copolymers in non-traditional lithography, these structures may expand the tools to provide more complex patterns.

5-6 References

1. Liu, C.-C.; Thode, C. J.; Delgadillo, P. A. R.; Craig, G. S. W.; Nealey, P. F.; Gronheid, R. *Journal of Vacuum Science & Technology B* **2011,** 29, (6).

2. Hong, A. J.; Liu, C.-C.; Wang, Y.; Kim, J.; Xiu, F.; Ji, S.; Zou, J.; Nealey, P. F.; Wang, K. L. *Nano Letters* **2010,** 10, (1), 224-229.

3. Jeong, S.-J.; Moon, H.-S.; Shin, J.; Kim, B. H.; Shin, D. O.; Kim, J. Y.; Lee, Y.-H.; Kim, J. U.; Kim, S. O. *Nano Letters* **2010,** 10, (9), 3500-3505.

4. Stoykovich, M. P.; Muller, M.; Kim, S. O.; Solak, H. H.; Edwards, E. W.; de Pablo, J. J.; Nealey, P. F. *Science* **2005,** 308, (5727), 1442-1446.

5. Kang, H.; Stuen, K. O.; Nealey, P. F. *Journal of Photopolymer Science and Technology* **2010,** 23, (2), 297-299.

6. Stuen, K. O.; Detcheverry, F. A.; Craig, G. S. W.; Thomas, C. S.; Farrell, R. A.; Morris, M. A.; de Pablo, J. J.; Nealey, P. F. *Nanotechnology* **2010,** 21, (49).

7. Liu, G.; Stoykovich, M. P.; Ji, S.; Stuen, K. O.; Craig, G. S. W.; Nealey, P. F. *Macromolecules* **2009,** 42, (8), 3063-3072.

8. Stoykovich, M. P.; Edwards, E. W.; Solak, H. H.; Nealey, P. F. *Physical Review Letters* **2006,** 97, (14).

9. Stuen, K. O.; Thomas, C. S.; Liu, G.; Ferrier, N.; Nealey, P. F. *Macromolecules* **2009,** 42, (14), 5139-5145.

10. Hashimoto, T. *Macromolecules* **1982,** 15, (6), 1548-1553.

11. Edwards, E. W.; Stoykovich, M. P.; Nealey, P. F.; Solak, H. H. *Journal of Vacuum Science & Technology B: Microelectronics and Nanometer Structures* **2006,** 24, (1), 340-344.

12. Court, F. o.; Hashimoto, T. *Macromolecules* **2001,** 34, (8), 2536-2545.

13. Sivaniah, E.; Matsubara, S.; Zhao, Y.; Hashimoto, T.; Fukunaga, K.; Kramer, E. J.; Mates, T. E. *Macromolecules* **2008,** 41, (7), 2584-2592.

14. Wu, Z. Q.; Li, B. H.; Jin, Q. H.; Ding, D. T.; Shi, A. C. *Macromolecules* **2011,** 44, (6), 1680-1694.

15. Yamaguchi, D.; Hashimoto, T. *Macromolecules* **2001,** 34, (18), 6495-6505.

16. Mickiewicz, R. A.; Ntoukas, E.; Avgeropoulos, A.; Thomas, E. L. *Macromolecules* **2008,** 41, (15), 5785-5792.

17. Papadakis, C. M.; Mortensen, K.; Posselt, D. *The European Physical Journal B - Condensed Matter and Complex Systems* **1998,** 4, (3), 325-332.

18. Matsen, M. W. *Journal of Chemical Physics* **1995,** 103, (8), 3268-3271.

19. Hashimoto, T.; Yamasaki, K.; Koizumi, S.; Hasegawa, H. *Macromolecules* **1993,** 26, (11), 2895-2904.

20. Morita, H.; Kawakatsu, T.; Doi, M.; Yamaguchi, D.; Takenaka, M.; Hashimoto, T. *Macromolecules* **2002,** 35, (19), 7473-7480.

21. Kane, L.; Satkowski, M. M.; Smith, S. D.; Spontak, R. J. *Macromolecules* **1996,** 29, (27), 8862-8870.

22. Hashimoto, T.; Koizumi, S.; Hasegawa, H. *Macromolecules* **1994,** 27, (6), 1562-1570.

23. Zhang, J.; Posselt, D.; Smilgies, D.-M.; Perlich, J.; Kyriakos, K.; Jaksch, S.; Papadakis, C. M. *Macromolecular Rapid Communications* **2014,** 35, (18), 1622-1629.

24. Jeong, U.; Ryu, D. Y.; Kho, D. H.; Lee, D. H.; Kim, J. K.; Russell, T. P. *Macromolecules* **2003,** 36, (10), 3626-3634.

25. Han, E.; Gopalan, P. *Langmuir* **2009,** 26, (2), 1311-1315.

26. Shin, C.; Ahn, H.; Kim, E.; Ryu, D. Y.; Huh, J.; Kim, K.-W.; Russell, T. P. *Macromolecules* **2008,** 41, (23), 9140-9145.

Chapter 6:

Conclusion

The unifying theme of this work has been to improve capabilities of BCP lithography by better understanding the design considerations for the chemical pattern and BCP formulation. In order to prepare block copolymer lithography for high-volume manufacturing, every parameter of the system will need to be optimized in order to meet the high demands for production. However, the prospect of a cheaper alternative to self-aligned multiple patterning and extreme ultraviolet lithography motivates the detailed study of BCP DSA.

The ideal chemical pattern for the well-ordered arrays of vertical lamellae that were targeted in this work would be stripes of PS and PMMA at the natural periodicity of the BCP. However, in order to employ DSA for resolution enhancement of photolithography, the lithographic pattern used to fabricate the chemical pattern must be a multiple of the natural periodicity of the BCP. Also standard application of lithography templates creates a binary pattern corresponding to the presence or absence of resist. The three-tone chemical patterns described in Chapter 2 capitalize on the difference in etch rate between the resist and the guide stripe material to form sidewall surfaces that switches which block is preferentially wetting due to the exposure to the plasma etch. This serendipitous intersection of conditions is only a glimpse of the possibility for three-tone patterns. In particular, the guiding surfaces are only weakly preferential to the respective blocks because UV light from the plasma etch modifies the X-PS and the brush material grafts a partial layer. As demonstrated in Chapter 3, less-preferential guide stripes negatively impacts the performance metrics of defect annihilation kinetics and line edge roughness. The controlled

reduction in wetting selectivity was used to quantify the impact of the wetting behavior of the guide stripes, but also points toward large gains available by minimizing the loss of selectivity during chemical pattern fabrication.

The focus of materials and process improvements for DSA should not be restricted to the chemical pattern but also include the BCP formulation. Parameter space in polymer blends is truly immense; the properties of the resulting formulation can be tailored with fine control. This work probed the behavior of two formulation systems. Chapter 4 addressed BCP + HP binary blends as an approach to assess composition asymmetry in DSA. The sensitivity of defect modes to the formulation study demonstrates the importance of controlling the overall volume fraction more than the bulk BCP phase diagram suggests. More detailed analysis is needed to investigate the 3D nature of the microbridge structures in the PS-rich formulation and to better understand the asymmetry dependence on the mechanism for misalignment annihilation. Also, different formulation approaches should be evaluated for tuning the periodicity and composition of the BCP and how they impact performance metrics such as defectivity and line roughness. The formulation system evaluated in Chapter 5 was macrophase-separating BCP + BCP binary blends of the same chemistry. The phase diagram shows that the blends become more miscible in films compared to bulk in both molecular weight ratio and volume fraction, even when the film is much thicker than the periodicity of the microdomains. Future work should aim to harness the macrophase separation regime into well-defined arrays using multiple periodicities using chemo- or graphoepitaxial alignment strategies. It may also be of interest to study the phase diagram as the large period phase is stretched or compressed in order to evaluate the relative magnitude of free energy involved in the macrophase separation process.